



Master's Thesis

Heat Transfer Simulations of Crevassed Glaciers

Max Nüßle

Longyearbyen, Norway and Stuttgart, Germany
July 2021

University of Stuttgart
Institute of Aerospace Thermodynamics
Prof. Dr.-Ing. Bernhard Weigand
Pfaffenwaldring 31
70190 Stuttgart
Germany

Norwegian University of Science and Technology
Department of Engineering Cybernetics
Dr. Richard Hann
O. S. Bragstads plass 2D
7034 Trondheim
Norway

University Center in Svalbard
Department of Geophysics
Dr. Marius Jonassen
P.O. Box 156
9171 Longyearbyen
Norway

Acknowledgements

I learned a lot in the last few months: things about simulations, things about writing, things about glaciers, nature, the Arctic, telemarking and a little too much about snowmobiles. Thank you to all the people who made this possible and supported me.

A big thanks to my supervisor Richard Hann at NTNU, who proposed this thesis to me, when I didn't even know it was possible to go to Svalbard. Thank you for the great supervision during the thesis, your help and support when I was unsure of what to do and for keeping me on track. Thank you to Marius Jonassen for the valuable feedback during our meetings, for always being helpful and being the contact at UNIS. This thesis wouldn't have been possible without Prof. Bernhard Weigand at the ITLR in Stuttgart who accepted me as his master student. Thank you as well for the discussions and feedback throughout my thesis.

Just the thesis and Svalbard would have been a good time. But what made it a great time, were all the people I got to know. Thank you to all my friends, who showed me around, who I went on trips with and who I got to spend my time in the office and in the kitchens with. Thank you for teaching me about pingos, sediment plumes, microplastic, bacteria, landforms, aurora, woollen base layers, snowmobiles, fjellski and so much more. I am especially grateful for the supportive and positive atmosphere in the Brakke, the sofas and the office. Without you, the Arctic would have been a cold and sad place.

Last, but not least I would like to thank all the software developers and IT people that keep everything running. Without you, nothing would get done. Thanks to POINTWISE for providing a license for their product, thank you to ANSYS, to the developers of L^AT_EX and Python. The last program I would like to express my gratitude to is the ERASMUS program for giving me money in exchange for some paperwork.

Abstract

Global warming and the associated melting of glaciers all around the world are accelerating. The water masses originating from glaciers will impact nature in multiple ways. Modelling the mass loss of glaciers can be done via modelling the surface energy balance. To gain insights into the spatial distribution of atmospheric heat transfer on a glacier, computational fluid dynamics (CFD) simulations are employed. The simulation software ANSYS FLUENT is used to simulate wind flowing over a cross-section of a glacier. The code is validated against experimental wind tunnel experiments for atmospheric boundary layer flow. The validation shows that with the $k-\omega$ SST and Spalart-Allmaras turbulence models can resolve trends, but overestimate heat transfer. For simulations on the glacier geometry with the Spalart-Allmaras turbulence model, the chosen boundary conditions show deficits in recreating an atmospheric boundary layer. Nevertheless, the results show that the heat transfer in heavily crevassed parts of the glacier is lower than on flat parts of the glacier. This is in contrast to the assumptions made in established surface energy balance models. The set-up and boundary conditions need to be refined, but can in principle be applied to any glacier.

Kurzfassung

Durch die globale Erwärmung schmelzen Gletscher und Eismassen auf der ganzen Welt immer schneller. Die Effekte des Abschmelzens werden unsere Umwelt nachhaltig verändern. Der Masseverlust kann über die Energiebilanz der Oberfläche modelliert werden. Um Modelle zur Energiebilanz zu verbessern und räumlich aufzulösen, bieten sich Simulationen (computational fluid dynamics, CFD) an. Das verwendete Simulationstool ANSYS FLUENT wurde gegen Experimente aus der Literatur auf seine Anwendbarkeit auf die Simulation von atmosphärischen Grenzschichten validiert. Die Validierung zeigt, dass mit den Turbulenzmodellen $k-\omega$ SST und Spalart-Allmaras der Wärmeübergang qualitativ dargestellt werden kann, jedoch quantitativ überschätzt wird. Bei 2D-Simulationen auf der Gletscheroberfläche mit dem Spalart-Allmaras Turbulenzmodell zeigen sich Schwächen in den gewählten Randbedingungen. Im Gegensatz zu den üblichen Modellierungsansätzen sagt die Simulation einen geringeren Wärmeübergang in stark zerfurchten Zonen gegenüber flachen Zonen voraus. Ähnliche Simulationsansätze lassen sich auf beliebige Gletscher anwenden.

Contents

List of Figures	VI
List of Tables	VIII
1. Introduction	1
1.1. Motivation	1
1.2. Glaciers, Mass and Energy Balance	1
1.3. Objectives	4
2. Methods	5
2.1. Modelling of Glacier Processes	5
2.2. Numerical Methods	6
2.2.1. Grid Generation	6
2.3. Equations of Fluid Flow	7
2.3.1. Navier-Stokes Equations	7
2.3.2. RANS Equations	8
2.4. Turbulence Modelling	8
2.4.1. k - ε Turbulence Models	10
2.4.2. k - ω Turbulence Model	10
2.4.3. k - ω SST Model	11
2.4.4. Spalart-Allmaras Model	12
2.5. Boundary Conditions	12
2.5.1. Velocity Profile	13
2.5.2. Temperature Profile	14
2.5.3. Turbulent Quantities	14
2.6. Heat Transfer	15
2.7. Geometry and Digital Elevation Modelling	15
2.8. Validation	16
2.8.1. Atmospheric Boundary Layer Flow	16
2.8.2. Heat Transfer	17
3. Simulations and Results	19
3.1. Validation	19
3.1.1. Atmospheric Boundary Layer on a Hill	19
3.1.2. Heat Transfer on Periodic Obstacles	22

3.2. 2D Simulations	25
3.2.1. Turbulence and Atmospheric Boundary Layer	28
3.2.2. Heat Transfer	29
3.2.3. Velocity Profiles	31
4. Discussion	36
4.1. Validation	36
4.2. Glacier Simulations	37
4.2.1. Atmospheric Boundary Layer	38
4.2.2. Heat Fluxes	38
4.3. Boundary Conditions	39
4.4. Geometry	39
4.5. Modelling	40
4.6. Possibilities for Improvement	41
4.7. Implications for Surface Energy Balance Modelling	42
5. Conclusion and Outlook	43
Bibliography	45
A. Appendix: Set-up and Grids	51
A.1. 2D Glacier	51
A.1.1. Meshes	51
A.1.2. Solver Set-Up and Boundary Conditions	51

List of Figures

1.2.1.	The heavily crevassed terminus of Fridtjovbreen, Svalbard on 8.5.2021.	2
1.2.2.	Mass and energy fluxes of an idealized glacier system [6].	3
2.7.1.	Mapped area of Fridjovbreen [46] and its location on Svalbard [47].	16
3.1.1.	Example T-Rex mesh for the Ishihara et al. validation case. Prism layer on the wall with refinement around the hill.	20
3.1.2.	Velocity profiles at different locations in the domain. Obtained with the $k-\omega$ SST model with experimental data [58]. Horizontal velocity on the top and vertical velocity on the bottom.	21
3.1.3.	Velocity profiles at different locations in the domain. Obtained with the Spalart-Allmaras model with experimental data [58]. Horizontal velocity on the top and vertical velocity on the bottom.	22
3.1.4.	Cut through the mesh of the Liu et al. [59] validation case.	23
3.1.5.	Surface temperatures on the fifth cube according to $k-\omega$ SST model and comparison with experimental and simulation data from [59].	24
3.2.2.	Mesh of the 2D simulations for the ‘flat’ case.	27
3.2.3.	Profiles of flow quantities at the inlet and outlet of an empty 2D domain without solving the energy equation. Horizontal velocity u_x on the left, turbulent viscosity ν_t on the right. $y_1^+ \approx 4$	29
3.2.4.	Turbulent viscosity ν_t on the flat glacier geometry with $\Delta_1 = 1$ mm.	29
3.2.5.	Turbulent viscosity ν_t on the step glacier geometry with $\Delta_1 = 1$ mm.	30
3.2.6.	Heat flux q and y_1^+ on the flat glacier geometry. The left side shows a relatively flat part of the glacier, while the right part shows a more crevassed part. The surface contour can be seen in the bottom.	31
3.2.7.	Heat flux q and y_1^+ on the step glacier geometry. The left side shows a relatively flat part of the glacier, while the right part shows a more crevassed part. The surface contour can be seen in the bottom.	32
3.2.8.	Velocity components in height y' over the glacier surface at two different locations with different cases.	33
3.2.9.	Velocity vectors in a crevasse on the flat geometry with $\Delta_1 = 1$ mm.	34
3.2.10.	Velocity magnitude on the flat geometry in three sections.	34
3.2.11.	Velocity profiles and fit at $x = 1060$ m (end of the glacier).	35
4.5.1.	Spatial variability of surface features on a glacier. Snow, meltwater and rocks on Longyearbreen, Svalbard. Taken on 27.07.2021	41

A.1.1. Overview of the flat mesh.	52
A.1.2. Overview of the step mesh.	52
A.1.3. Detail close with the end of the step glacier geometry.	53
A.1.4. Detail at the beginning of the step glacier geometry at 0 m.	53

List of Tables

3.2.1. Boundary conditions of the 2D cases.	28
3.2.2. Average heat flux for the sections shown in Figures 3.2.6 and 3.2.7, an additional section close to the terminus and the whole glacier surface. Values for the investigated mesh geometries with $\Delta_1 = 1$ mm.	33
A.1.1. T-Rex set-up for flat and step case	51
A.1.2. Boundary conditions for flat and step case	52
A.1.3. Solver set-up for 2D glacier cases.	53

List of Symbols

Symbol	Unit	Description
δ	m	boundary layer thickness
δ_{ij}	–	Kronecker-delta
ε	s^{-1}	dissipation rate
η	Nsm^{-2}	dynamic viscosity
κ	–	von Kármán constant
ν	m^2s^{-1}	kinematic viscosity
ν_t	m^2s^{-1}	turbulent viscosity
ω	s^{-1}	turbulent frequency
ρ	kgm^{-3}	density
τ	Nm^{-2}	shear stress
θ	ms^{-2}	shear velocity
e	Jkg^{-1}	specific energy
k	Jkg^{-1}	turbulent kinetic energy
p	Pa	pressure
q	Wm^{-2}	heat flux
Q	J	heat
Re	–	Reynolds number
t	s	time
T	K, °C	temperature
u	ms^{-1}	velocity
x, y, z	m	coordinates
y^+	–	dimensionless wall distance

1. Introduction

1.1. Motivation

Climate change and its effects are undoubtedly one of the biggest challenges we have to overcome in the next decades and centuries. The impact of human civilisation has shaped the nature around us since the beginning. However, in the last centuries the impacts that humanity has on the environment have outgrown the effects of every other species that has lived on earth [1, 2].

By releasing climate active gasses, the radiation balance of earth is affected significantly which will lead to rising temperatures in the atmosphere [1]. One region which is especially affected by the change in temperatures is the Arctic [1, 3]. The temperature in the Arctic has risen at least twice as fast as in other places. This effect is also known as Arctic amplification [3].

Large ice sheets in Greenland and the arctic island Svalbard are directly impacted by climate change [4]. Rising temperatures and changing climatic conditions already have an impact on the mass balance on these glaciers [4]. On a larger scale, mass loss from ice caps and glaciers will contribute to the global sea level rise and lower the salinity of sea water, impacting ocean currents [5, 6]. A sound understanding on the processes involved in the melting-off in the polar regions is crucial for modelling the challenges to come.

1.2. Glaciers, Mass and Energy Balance

The growing and shrinking of glaciers is governed by a wide range of effects and processes. Usually, glaciers gain mass by precipitation, avalanches from terrain higher up or wind drifted snow. The ice mass is transported downhill by the flow of the glacier [6].



Fig. 1.2.1.: The heavily crevassed terminus of Fridtjovbreen, Svalbard on 8.5.2021.

In zones with high stresses in the ice, the ice can fracture and crevasses can develop. Such zones of high stress might emerge when the glacier flows over changing terrain or terminates at the sea [7]. This, for example, is the case at Fridjovbreen, seen in Figure 1.2.1. Note that the crevasses are generally aligned with the glacier front.

Modelling the movement, mass accumulation and mass loss of glaciers and ice caps therefore includes a wide range of physical effects. Most of these, like precipitation, solar radiation and temperature, might differ from year to year and can only be approximated coarsely [8, 9]. Multiple approaches have been developed to tackle this complex task of modelling mass balance ranging from relatively simple statistical approaches to more and complicated and spatially resolved models [10].

To gauge the melting of the glacier ice on the surface, knowledge about the surface energy balance is necessary. A schematic of different energy and mass fluxes can be seen in Figure 1.2.2. As soon as the snow or ice on the surface reaches 0°C , every additional energy results in the melting of the ice or snow. In the context of glaciers, the energy fluxes are divided in latent heat and sensible heat. In more common thermodynamic terms, latent heat would be called enthalpy. Latent heat could be released or consumed by the melting of ice and the refreezing of water in the glacier. Sensible heat fluxes are, for example, heat fluxes from the earth below the ice, short and long wave radiation or aerodynamic heat transport to and from the surface. These aerodynamic heat fluxes are increased by turbulent mixing in the atmosphere [6, 8].

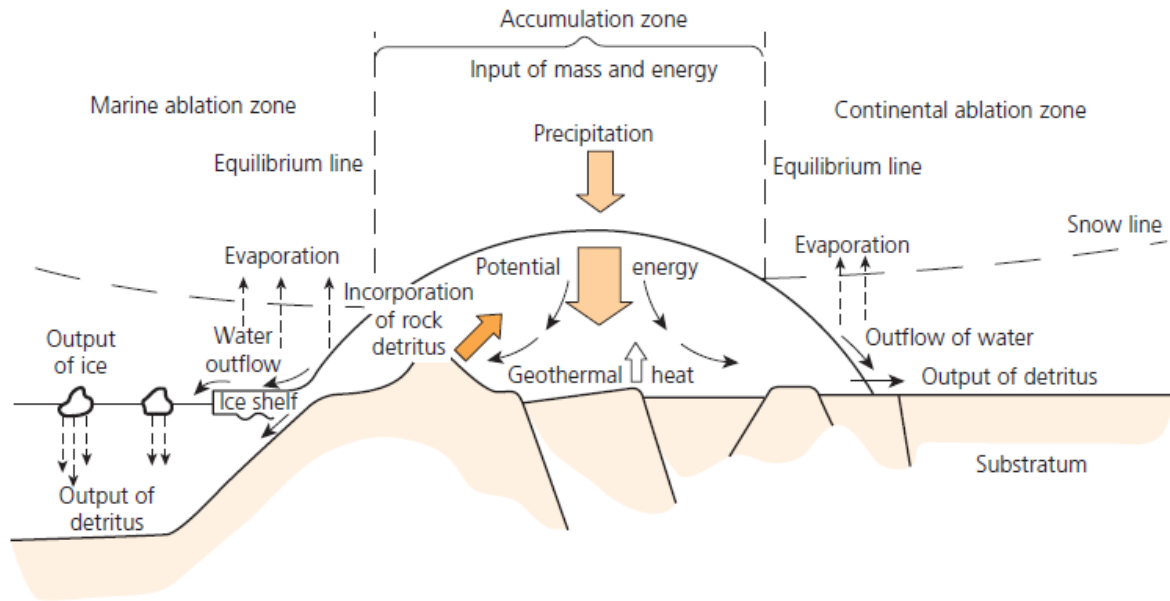


Fig. 1.2.2.: Mass and energy fluxes of an idealized glacier system [6]

Direct heat exchange between the atmosphere and the glacier surface is increased by mixing the air due to turbulence. Warming of the atmosphere might increase the importance of turbulent heat fluxes in the energy balance [11]. However, these heat fluxes might be underestimated in common modelling approaches [11]. From an engineering standpoint, we should be able to model these fluxes via established computational fluid dynamics (CFD). The development of the turbulent boundary layer is heavily influenced by the surface geometry. The increase of surface roughness should lead to more turbulent mixing and therefore more heat convective heat transfer.

This dependency on the surface roughness is also represented in common surface energy balance models. The turbulent heat transfer in those models is largely dependent on the aerodynamic roughness height as a parameter [8]. However, the roughness height of the glacier surface is not uniform as some models assume. Therefore the heat transfer changes depending on the location on the glacier. In earlier work, two different approaches were taken to quantify the changing roughness height. Dachauer et al. calculated the roughness height from digital elevation models [12]. Garreau estimated the boundary layer profile on the glacier from drone data [13]. From this data it is possible to estimate the roughness height of the surface.

The modelling of turbulent fluxes in the surface energy balance model might be improved by improving the estimation for the surface roughness, but surface energy balance models generally don't give spatially resolved results [6]. Insights in the small-scale variations

of the turbulent fluxes can be gained by numerical simulation of the flow field and heat transfer.

1.3. Objectives

To gain insights into the spatial distribution of turbulent heat transfer, a crevassed glacier surface will be investigated. For this, fluid dynamics simulations of the atmosphere above the glacier have to be set up. Suitable boundary conditions and approaches for modelling need to be found. The simulation methods and used software need to be validated in order to gain trust in the results.

Applying these boundary conditions with the validated code to a glacier surface should yield first insights into the heat transfer due to turbulent fluxes. For initial simulations and set-up, two-dimensional simulations should suffice, while for more detailed investigations three-dimensional simulations should be used.

With the methods and approaches developed in this thesis, it should be possible to apply these to geometries of different glaciers or ice sheets. Results from similar simulations could be used to improve the modelling of surface energy balance and therefore the modelling of melting of glaciers.

2. Methods

2.1. Modelling of Glacier Processes

Modelling the heat transfer between a glacier surface and the atmosphere above involves modelling processes taking place in the atmosphere and in the ice mass, as well as below (see Section [1.2](#)).

Especially scale differences between mechanisms like the impingement of a warm raindrop on the cold ice and the crevasses disturbing the wind make it challenging to model heat transfer on a glacier surface accurately. Therefore, to keep the simulation feasible and first results achievable, some simplifications have to be made. In this thesis, the modelling is limited to the heat fluxes through the glacier surface due to turbulent mixing and the wind blowing over the glacier surface. Most fluid flow, including winds, can be described by the Navier-Stokes equations. A more detailed description about these equations and their modelling is given in Section [2.3](#).

The influence of liquid water on the surface, as well as phase change phenomena and the latent heat released or bound by these phenomena is neglected. This is done by considering the surface of the glacier as a solid wall. This also means, that the surface is not changing due to depositions of snow or melting of ice or the flow of water.

Neglecting phase change on the surface also allows to neglect the influence of water vapour in the airflow and related changes of density and heat capacity. Not considering the vapour content of the air makes it possible to model the air as single phase.

Temperature gradients in the ice, as well as heat fluxes due to melting and refreezing inside the ice mass are not considered. Furthermore, geothermal heat fluxes from the earth into the ice are not considered, too. The ice surface is considered to be at a fixed temperature.

2.2. Numerical Methods

Due to the complexity of the Navier-Stokes equations only approximate solutions can be obtained for most cases. There are multiple numerical methods for solving systems of partial differential equations. Usually, flow problems are solved by applying the finite-volume method. This method guarantees the conservation of momentum and mass flow through the domain [14].

Multiple commercial and research-oriented software packages exist, which solve the Navier-Stokes equations and provide an interface to the user. For this thesis ANSYS FLUENT 2020 R1 is used. ANSYS FLUENT is widely used in CFD applications and provides a tool-chain from meshing to post-processing. For most cases in this thesis, however, it is only used for solving the momentum equations.

2.2.1. Grid Generation

For solving the Navier-Stokes equations numerically, the underlying geometry has to be discretized. Generally, grids can be divided in two basic types: Structured and unstructured. In structured grids, the neighbouring grid points or cells can be inferred from the current grid cell. In contrast to unstructured grids, a list has to be kept in memory, where the neighbours of every cell are stored. Therefore, the memory demand for unstructured grids is typically higher compared to structured grids. The cells used in unstructured grids can have different shapes which are easier to fit to complex geometries. In general, structured grids can be transformed to fit a wide range of geometries as well, but the computation of these transformations is costly in computational time. This leads to less generation time on complex geometries for unstructured grids. Mainly due to that, unstructured grids are dominating in industrial applications [14].

The meshing process is usually done with specific software tools. The meshes in this thesis were made with the software POINTWISE V18.4R2 [15]. With POINTWISE structured and unstructured meshes can be generated. To improving the resolution in the boundary layer, a hybrid mesh approach can be used. Cells at the surface should be relatively flat to resolve the strong gradients normal to the surface. This can be done with a prism layer, growing into larger cells further away from the wall and transforming into a fully unstructured grid in the free-stream. For this, POINTWISE offers the T-Rex algorithm (short for tetrahedral right-angle extrusion). The T-Rex algorithm allows

to grow prism layers from the surface and stops growing these prism layers when two advancing fronts are about to collide [16].

2.3. Equations of Fluid Flow

2.3.1. Navier-Stokes Equations

The Navier-Stokes equations are a system of partial differential equations, which describe fluid flow problems. These equations are of special interest to engineers and physicists, because they provide solutions for compressible viscous fluid flows over a large range of flow velocities, viscosities and other flow parameters [17].

Mathematically, the Navier-Stokes equations are derived from conservation of mass and conservation of momentum. This derivation is done assuming a linear relationship between shear stress τ and shear velocity $\frac{du}{dy}$. For Newtonian fluids, the shear stress tensor can be stated as

$$\tau_{ij} = \tau_{ji} = 2\eta\vartheta_{ij} \quad (2.3.1)$$

with the dynamic viscosity η and the strain rate

$$\vartheta_{ij} = \frac{1}{2} \left(\frac{\partial u_j}{\partial x_i} + \frac{\partial u_i}{\partial x_j} \right) \quad (2.3.2)$$

This means that the Navier-Stokes equations are only valid for Newtonian fluids, where this assumption holds [17].

The Navier-Stokes equations state the conservation equations for momentum (Equation 2.3.3). For a complete physical description of the flow, the conservation of mass (Equation 2.3.4) is needed. The system is closed by the energy equation (Equation 2.3.5). Additionally, the conservation of energy is also linked to the caloric equation of state of the fluid. The full set of equations can be stated as

$$\frac{\partial}{\partial t}(\rho u) + \nabla \cdot (\rho u \times u) - \nabla p = \nabla \cdot \tau + g \quad (2.3.3)$$

$$\frac{\partial}{\partial t}\rho + \nabla \cdot (\rho u) = 0 \quad (2.3.4)$$

$$\frac{\partial}{\partial t}e + \nabla \cdot (u(e + p)) = \nabla \cdot (\tau u) - \nabla \cdot q + Q \quad (2.3.5)$$

2.3.2. RANS Equations

For most engineering applications, it is too costly in terms of computational resources to compute solutions of fully resolved Navier-Stokes equations. In a large number of cases, it is sufficient to obtain the mean solution averaged over a time period because in an engineering context conditions are usually not changing rapidly all of the time [14].

Time averaging of the Navier-Stokes equations leads to the Reynolds-averaged Navier-Stokes (RANS) equations. This results in additional unknown terms. These are the so called Reynolds stresses $\overline{\rho u'_i u'_j}$ and the turbulent energy flux $\rho c_p \overline{u'_i T'}$. For closure of the newly obtained system, these terms have to be modelled [18].

2.4. Turbulence Modelling

For closing the system of the RANS equations, modelling of the Reynolds stresses and turbulent energy flux is necessary. There are two main approaches to modelling these terms. In eddy-viscosity type models, the Reynolds stresses are related to the mean velocity gradients. For this to work, the turbulent stress tensor is assumed to be equal to the laminar stress tensor. It can be stated as

$$\overline{u'_i u'_j} = -\nu_t \left(\frac{\partial \overline{u}_i}{\partial x_j} + \frac{\partial \overline{u}_j}{\partial x_i} \right) + \frac{2}{3} \delta_{ij} k \quad (2.4.1)$$

, with the turbulent kinetic energy k , the turbulent viscosity ν_t and the Kronecker-delta δ_{ij} . This assumption is also known as Boussinesq-hypothesis [18].

The Boussinesq-hypothesis implies that turbulence is isotropic. This is adequately accurate for a large number of flows, but especially the generation of turbulence can be highly anisotropic. In cases with large separation areas where production of turbulence is high, the models show shortcomings [19]. This includes recirculations zones, detached flow and flow impingement.

For closing the system, eddy viscosity models model the eddy viscosity ν_t . From dimensional analysis it is known that ν_t is proportional to a length scale l and velocity scale u . Therefore, the ν_t can be either modelled directly by modelling l or u . This can be done algebraically or via transport equations. Algebraical turbulence models, also called zero-equation models, are simple and robust in their implementation, but are only applicable for a narrow range of problems with simple geometries [20, 21].

Modelling the transport of ν_t via differential equations allows for a wider range of geometries. One-equation models estimate ν_t directly while two-equation models model the length scale and velocity scale with separate equations [20].

In contrast to the eddy-viscosity type models, Reynolds-stress models directly model the transport of the Reynolds stresses. This type is generally considered to be more accurate because of its more complete description of the flow. This makes them tend to be more precise in complex flow situations and when body forces on the fluid have to be considered [19]. But on the downside they are computationally more expensive because a system of seven equations has to be solved in contrast to up to two equations for established eddy-viscosity type models. They also tend to be less stable [22, 23].

Because flow quantities usually have strong gradients near walls, special attention has to be paid to the wall-treatment in turbulence models. The boundary layer near the wall can be divided into different sections depending on the wall distance [24, 25]. Usually, this division is done in dimensionless variables friction velocity u_τ derived from the wall shear stress τ_w and the dimensionless wall distance y^+ . The kinematic viscosity of the fluid is denoted by ν . The friction velocity and dimensionless wall distance can be computed as

$$u_\tau = \sqrt{\frac{\tau_w}{\rho}} \quad (2.4.2)$$

$$y^+ = \frac{yu_\tau}{\nu} \quad (2.4.3)$$

For fully developed turbulent wall flows, the velocity profile can be approximated by wall functions [14, 25]. The usage of wall functions allows resolving of the boundary layer with less grid cells close to the wall [14]. The use of wall functions on grids with $y_1^+ < 15$ might lead to numerical instability, but ANSYS FLUENT employs mitigations against that [25].

A selection of eddy-viscosity-type models will be described. These models are among the most commonly used and are also good prospects for modelling in this thesis. Eddy viscosity models usually contain terms describing the production, destruction and the redistribution of turbulence. This is done in partial differential equations describing the transport of the turbulent quantities through the domain and their time evolution.

2.4.1. k- ε Turbulence Models

A widely used class of turbulence models are the k- ε turbulence models. These turbulence models proved to be very popular in the last decades [20] and also have a variety of formulations. The standard formulation of the k- ε model is the formulation of Launder and Spalding [26]. The transport equations of the model can be given as

$$u_j \frac{\partial k}{\partial x_j} = \frac{\partial}{\partial x_j} \left(\frac{\nu_t}{\sigma_k} \frac{\partial k}{\partial x_j} \right) + P_k - \varepsilon \quad (2.4.4)$$

$$u_j \frac{\partial \varepsilon}{\partial x_j} = \frac{\partial}{\partial x_j} \left(\frac{\nu_t}{\sigma_\varepsilon} \frac{\partial \varepsilon}{\partial x_j} \right) + C_{\varepsilon_1} \frac{\varepsilon}{k} P_k - C_{\varepsilon_2} \frac{\varepsilon^2}{k} \quad (2.4.5)$$

with the production term

$$P_k = \nu_t \frac{\partial u_i}{\partial x_j} \left(\frac{\partial u_i}{\partial x_j} + \frac{\partial u_j}{\partial x_i} \right) \quad (2.4.6)$$

The diffusion term for $k = \frac{\partial}{\partial x_j} \left(\frac{\nu_t}{\sigma_k} \frac{\partial k}{\partial x_j} \right)$ and the analogous term in the ε equation are chosen according to the gradient transport hypothesis, which links the diffusion of a quantity proportionally to its spatial gradient [21]. C_{ε_1} and C_{ε_2} are closure coefficients.

Especially at stagnation points, the turbulent kinetic energy is overestimated [27]. Other model variants, which are commonly used and try to mitigate against this overproduction include the k- ε RNG model by Yakhot et al. [28] and the realisable k- ε model by Shih et al. [29].

In the k- ε RNG model, the closure coefficients are determined by the mathematical method of renormalization group theory. It also employs extra terms for improving accuracy in flows with high strain rates and swirling flow [25, 28].

The realisable k- ε model tries to improve upon the standard formulation by introducing an alternative formulation for eddy viscosity including the effects of rotation as well as deriving exact ε -equation from the equation of mean-square vorticity fluctuation [25, 29].

2.4.2. k- ω Turbulence Model

A number of models have been developed which take the turbulent kinetic energy k and a frequency ω into account. ω can be interpreted as the frequency of the decay of

turbulence or simply as ε/k . An early version has been derived by Kolmogorov [30]. Over the years, the model has been altered and improved by Wilcox, e.g. [20, 31, 32]. The formulation derived by Wilcox [20] is also used in Ansys Fluent [25]. Its transport equations for k and ω are

$$\frac{\partial k}{\partial t} + u_j \frac{\partial k}{\partial x_j} = \tau_{ij} \frac{\partial u_i}{\partial x_j} - \beta^* k \omega + \frac{\partial}{\partial x_j} \left[\left(\nu + \sigma^* \frac{k}{\omega} \right) \frac{\partial k}{\partial x_j} \right] \quad (2.4.7)$$

$$\frac{\partial \omega}{\partial t} + u_j \frac{\partial \omega}{\partial x_j} = \alpha \frac{\omega}{k} \tau_{ij} \frac{\partial u_i}{\partial x_j} - \beta \omega^2 + \frac{\sigma_d}{\omega} \frac{\partial k}{\partial x_j} \frac{\partial \omega}{\partial x_j} + \frac{\partial}{\partial x_j} \left[\left(\nu + \sigma \frac{k}{\omega} \right) \frac{\partial \omega}{\partial x_j} \right] \quad (2.4.8)$$

A unique part of the k - ω model is the so-called cross-diffusion term $\frac{\sigma_d}{\omega} \frac{\partial k}{\partial x_j} \frac{\partial \omega}{\partial x_j}$. It stems from the derivation of the ω equation from the ε equation. This term needs to be limited in the free shear flow to an empirical value. This is done with a blending function in σ_d .

Experience shows that the k - ω model shows good behaviour in near-wall regions and in small adverse pressure gradients [33, 34]. However, the solution in the boundary layer is known to be sensitive to the initial turbulence values in the free stream [33, 35].

2.4.3. k - ω SST Model

The k - ω shear stress transport (SST) model by Menter [34] tries to combine the strengths of the k - ω model near the wall and the robustness of the k - ε model in the free stream region of the flow. This is achieved using a blending function between these models. Depending on the wall distance the blending function favours k - ω near the wall and k - ε further away from the wall. A small blending region exists in between [34]. The transport equations for k and ω are given as

$$\frac{\partial(\rho k)}{\partial t} + \frac{\partial(\rho u_i k)}{\partial x_i} = \tilde{P}_k - \beta^* \rho k \omega + \frac{\partial}{\partial x_i} \left[(\mu + \sigma_k \mu_t) \frac{\partial k}{\partial x_i} \right] \quad (2.4.9)$$

$$\frac{\partial(\rho \omega)}{\partial t} + \frac{\partial(\rho u_i \omega)}{\partial x_i} = \alpha \rho S^2 - \beta \rho \omega^2 + \frac{\partial}{\partial x_i} \left[(\mu + \sigma_\omega \mu_t) \frac{\partial \omega}{\partial x_i} \right] + 2(1 - F_1) \rho \sigma_{w2} \frac{1}{\omega} \frac{\partial k}{\partial x_i} \frac{\partial \omega}{\partial x_i} \quad (2.4.10)$$

The blending function F_1 blends between the k- ε in the freestream and k- ω model at the wall. It is given as

$$F_1 = \tanh \left\{ \left\{ \min \left[\max \left(\frac{\sqrt{k}}{\beta^* \omega y}, \frac{500\nu}{y^2 \omega} \right), \frac{4\rho\sigma_{\omega 2} k}{CD_{k\omega} y^2} \right] \right\}^4 \right\} \quad (2.4.11)$$

In a wide variety of cases the k- ω SST model shows good accuracy and good convergence behaviour [33].

2.4.4. Spalart-Allmaras Model

The turbulence model of Spalart and Allmaras [36] is an one equation turbulence model. It proved to be quick and reliable in convergence and forgiving in grid parameters [20, 36].

The Spalart-Allmaras model models a modified vortex viscosity $\hat{\nu}_t$. This modified vortex viscosity allows for easier numerical handling of the boundary layer [25]. The transport equation for the modified vortex viscosity in ANSYS FLUENT is given as

$$\frac{\partial}{\partial t}(\rho\tilde{\nu}) + \frac{\partial}{\partial x_i}(\rho\tilde{\nu}u_i) = G_v + \frac{1}{\sigma_{\tilde{\nu}}} \left[\frac{\partial}{\partial x_j} \left\{ (\mu + \rho\tilde{\nu}) \frac{\partial\tilde{\nu}}{\partial x_j} \right\} + C_{b2}\rho \left(\frac{\partial\tilde{\nu}}{\partial x_j} \right)^2 \right] - Y_v + S_{\tilde{\nu}} \quad (2.4.12)$$

G_v is the production of turbulent viscosity, Y_v its destruction term and $S_{\tilde{\nu}}$ a user-defined source term; $\sigma_{\tilde{\nu}}$ and C_{b2} are model constants [25].

Despite being developed for flows over aircraft wings with a low adverse pressure gradient [36], industrial experience has lead to wide-spread use.

2.5. Boundary Conditions

For a valid numerical solution, appropriate boundary conditions need to be set. In a fluid dynamics problem, this includes velocities, pressures, temperatures and turbulent quantities. Depending on the chosen turbulence model, different quantities need to be specified.

Especially for atmospheric boundary layer simulations, the boundary conditions for velocity and turbulent quantities need to match. Richards and Norris [23] specified a set of boundary conditions for different turbulence models that are sufficient to sustain their profiles in an empty domain without perturbations to the flow. However, even if those boundary conditions are applied thoroughly, the implementation in commercial codes like ANSYS FLUENT might not lead to sufficient results [37].

For generating the inlet conditions on glaciers in the Arctic little data is available. However, more data from the study of wind turbines and their environment can be found.

2.5.1. Velocity Profile

The velocity distribution in the lower part of the atmospheric boundary layer can be described in form of the log-law [18, 38]

$$\bar{u}(y) = \frac{u_\tau}{\kappa} \ln \left(\frac{y}{y_0} \right) \quad (2.5.1)$$

It uses the friction velocity u_τ (Equation 2.4.2), the roughness height y_0 and the von Kármán constant to approximate a mean velocity profile. The log-law for the velocity profile is derived with the assumption of a constant shear stress and a thermally neutral boundary layer [38]. The log-law gives appropriate results for neutral boundary layers and heights y larger than the surface roughness elements and smaller than 100 m [39].

When measurements are available, the log-law can be written in the form of

$$\bar{u}(y) = u_1 \frac{\ln \left(\frac{y}{y_0} \right)}{\ln \left(\frac{y_1}{y_0} \right)} \quad (2.5.2)$$

where u_1 designates the velocity measured at the height y_1 .

In preceding work, Dachauer et al. [12] investigated the roughness height on tide water glaciers using areal imagery. For flat areas on the glacier, roughness heights y_0 ranging down to 0.08 m were found. Since the glacier geometry in this thesis is quite flat, a value of $y_0 = 0.1$ m has been chosen.

2.5.2. Temperature Profile

In the troposphere and atmospheric boundary layer, the temperature of the air generally decreases with increasing height [38]. A common model for the temperature profile in engineering applications is specified in the ISO standard 2533 [40]. The equation reads as

$$T = T_0 + \beta (H - H_0) \quad (2.5.3)$$

with temperature T , base temperature $T_0 = 273.15$ K, geopotential altitude H and base altitude H_0 as well as the vertical temperature gradient β . The temperature gradient β is given in ISO 2533 as -6.5 K km⁻¹.

Similarly, extrapolating the surface temperatures from larger-scale climate models is often done with linear relations [41]. Gardner et al. [41] investigated multiple glaciers in the Canadian high Arctic. They conclude that calibrating the temperature gradient is necessary for different glaciers and seasons. For cases with insufficient data to calibrate, they suggest using a temperature gradient of -4.9 K km⁻¹. However, their data is specific to glaciers in the Canadian Arctic and weather and atmospheric conditions might not be comparable to Svalbard. The ISO 2533 gradient of 6.5 K km⁻¹ is also used in other research for downscaling models on Svalbard [42]. It lies well in the range of temperature gradients determined for some glaciers by Gardner et al. [40, 41].

2.5.3. Turbulent Quantities

The inlet conditions for turbulent quantities can be specified with different methods in ANSYS FLUENT. It is possible to specify the modelled quantities like e.g. k , ω or ν_t directly, but these can also be calculated by giving turbulence intensity, turbulent length scale and similar quantities [43].

The ANSYS FLUENT user guide suggests setting turbulent length scale and turbulent intensity for wall bounded flows. For the highest accuracy, profiles of these quantities should be specified. Literature suggestions are mostly tied to specific turbulence models and geared towards industrial applications [23]. Even with these boundary conditions applied, the implementation in the ANSYS FLUENT is not sufficient to sustain the inlet conditions in an empty domain [37].

In the ANSYS FLUENT user's guide it is recommended to choose the turbulent length scale as a characteristic length of the problem [43]. Studies of turbulent intensity (TI) on open water for wind parks suggest that intensities of $TI \approx 6\% \dots 10\%$ are realistic [44]. As the surface of a glacier is quite irregular, choosing a characteristic length is not straightforward. As an approximation, the depth of the crevasses is the model of $l \approx 5$ m is chosen.

2.6. Heat Transfer

Heat transfer describes the redistribution of thermal energy in space. Heat transfer can be separated into conduction, convection and radiation. While for conduction and convection movement of mass is necessary, radiative heat transfer occurs only by radiation. In conduction the thermal energy is transferred through matter without movement of mass and convection is the transport of thermal energy by the movement of matter.

In a fluid dynamics problem, conduction and convection of the thermal energy described by the energy equation in the Navier-Stokes equations (Equation 2.3.5). The heat transfer between fluid and solid is highly dependent on the characteristics of the boundary layer close to the surface [45]. Therefore, it is important to resolve this near-wall layer adequately.

2.7. Geometry and Digital Elevation Modelling

The surface geometry used in this thesis is of the tidewater glacier Fridtjovbreen, seen in Figure 2.7.1, in Nordenskiöldland on Svalbard, Norway. The glacier extends southwards towards Van Mijenfjorden and is about 10 km long. Its upper part is mostly flat, while its heavily crevassed close to the terminus. The geometry was captured by Dachauer et al. with digital elevation modelling [12].

Digital elevation models (DEMs) are a representation of local topography. Usually, it is given in a pixel format with the local elevation above a reference point for the pixel value [48]. Dachauer et al. used photogrammetry with aerial photographs obtained from drone flights. For a more detailed description on how these models were built and a discussion of the methods, see [12].

After preparing the files, the DEMs can be used as input geometry for meshing.

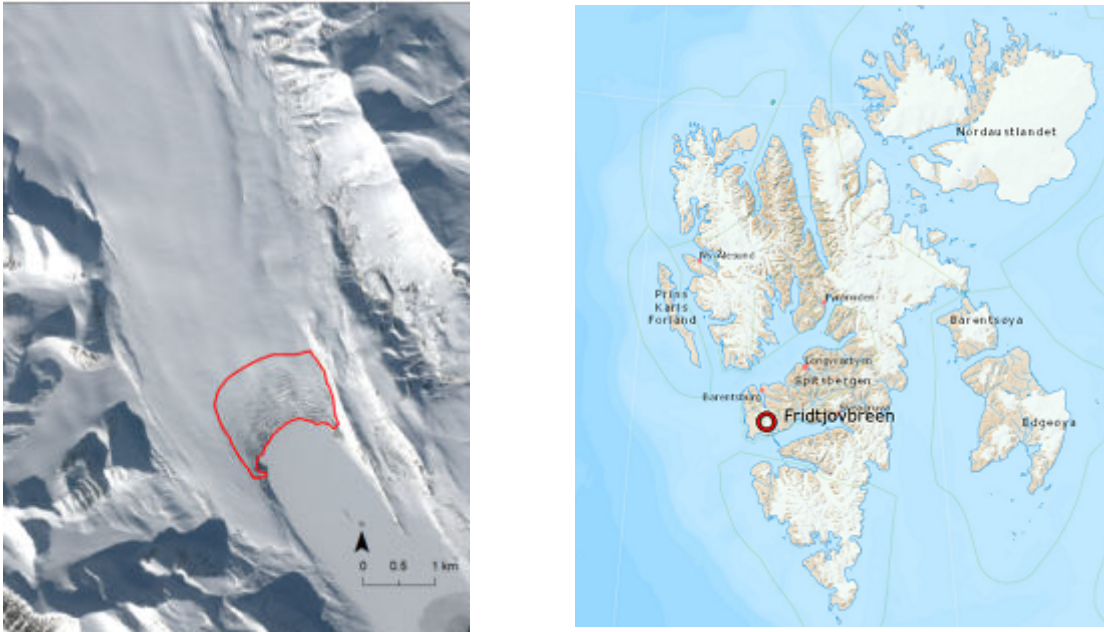


Fig. 2.7.1.: Mapped area of Fridtjovbreen [46] and its location on Svalbard [47].

2.8. Validation

Validation is making sure to solve the right equations with the right models and on suitable meshes [49]. This means showing that the selected models and equations represent the nature suitably well. Usually, this is done with comparing the computational results to a similar case that is well-known and characterized [49].

2.8.1. Atmospheric Boundary Layer Flow

There is a great interest in the industry to investigate atmospheric boundary layer flows across large terrain features to characterize wind fields for wind turbine placement [50–53]. Although these studies may give insight into the set-up of such atmospheric boundary layer simulations, the length scales which are of interest are much larger than the scales of crevasses on glaciers. An interesting field to look out for might be pedestrian wind engineering. This field tries to predict the wind pedestrians are expected to experience in cities and around buildings [54]. Although the buildings themselves might still be larger than the crevasses and structures found on glaciers, the sharp edges and complicated geometry might lead to similar modelling constraints.

Multiple measurement campaigns have been conducted to find suitable validation cases for wind speed in atmospheric boundary layer simulations. Most notably are the meas-

measurements at Askervein Hill in Scotland [55] and the Bolund Hill in Denmark [56]. Of special interest is the Bolund Hill, because the geometry and the measurement data are available [57]. Downwind of the Bolund Hill, a large area is covered by water. This leads to well-defined boundary conditions due to the lack of surface features and protrusions. Also the length scales of the Askervein Hill are significantly larger than the length scales on a crevassed glacier. The Bolund Hill is closer to those. However, both cases require a substantial effort in meshing and set up of the case due to their complex geometries and modelling of the complex wind patterns.

Easier validation cases to model are wind tunnel experiments with model hills. For these, analytically generated shapes like cosine waves are manufactured and examined in wind tunnels. These have the benefit of having clearly defined boundary conditions and geometry. Also, these experiments can be tailored to the requirements regarding Reynolds number and other flow variables. An interesting case to validate against is described by Ishihara et al. [58]. The length scales found in this case are the closest to the ones found on glaciers.

For checking if the boundary conditions are applied correctly, a domain without any perturbations can be simulated. If all the boundary conditions correct, the boundary layer profiles from the inlet are preserved over the whole length of the domain [23].

2.8.2. Heat Transfer

Finally, the heat transfer has to be validated as well because even though the flow field might match generally quite well, the heat transfer is dependent on the correct velocities close to the wall. Heat transfer is generally harder to measure and therefore harder to compare to. This means that cases for the validation of the heat transfer have to be found. For this, experiments geared towards aerodynamics and heat transfer on buildings are a good starting point. In Liu et al. [59], the authors investigate a case experimentally and numerically with large eddy simulation and RANS simulations with different turbulence models. The case consist of periodic cubes that are heated from the inside and placed in a wind tunnel. For determining heat transfer the surface temperatures of one of these cubes was measured.

All of those cases above share that they evaluate flow parameters and disturbance of those around geometries that perturb the flow. This is mostly not the case on the surface of crevassed glaciers, whose surface is characterized by deep grooves. Furthermore, there

are no investigations of heat transfer at the surface because the above mentioned studies mainly look at the application for wind power.

For this thesis the code has been validated with the cases by Ishihara et al., Liu et al. Those two cases capture roughly the same length scales as found on the glacier and have well-defined boundary conditions.

3. Simulations and Results

3.1. Validation

To validate the code for application of heat transfer on the glacier geometry, two cases are calculated. The chosen cases are experimentally investigated by Liu et al. [59] and Ishihara et al. [58]. A more detailed description is given in Section 2.8.

3.1.1. Atmospheric Boundary Layer on a Hill

For validating the code ANSYS FLUENT for atmospheric boundary layer simulations, the simulation results are compared to the experiment of Ishihara et al. [58]. Ishihara et al. have conducted a wind tunnel study of a hill with a \cos^2 -shape. The model hill corresponds to a intermediate height scale which makes is sufficiently similar to the scale of crevasses found on a glacier.

For turbulence modelling, the $k-\omega$ SST and Spallart-Alamaras turbulence models is used. The velocity profile on the inlet is specified as a user defined function according to the profile given in the paper by Ishihara et al.

The grid consists of regular prism cells on the wind tunnel floor as well as on the hill to resolve the boundary layer. The initial cell height at the wall was kept the same for all the generated meshes. This leads to a maximum y_1^+ of 0.1. Around the cube itself a finer resolution is applied to the grid to capture the more complex flow geometry. An example mesh is depicted in Figure 3.1.1. Within this general set-up multiple grids with different resolutions are generated. It is visible in the velocity profiles depicted in Figure 3.1.2, that for the $k-\omega$ SST model a jump between the grid with 10 million cells and the grid with 20 million cells exist. Therefore, a fourth resolution of 40 million cells is introduced to show grid independence. The Reynolds number based on the thickness of the boundary layer δ with the kinematic viscosity ν is $Re = u_\delta \delta / \nu = 1.4 \times 10^5$.

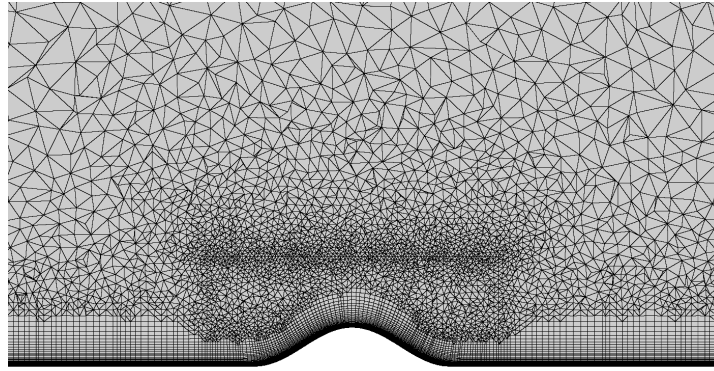


Fig. 3.1.1.: Example T-Rex mesh for the Ishihara et al. validation case. Prism layer on the wall with refinement around the hill.

Both turbulence models manage to capture the general shape of the velocity profiles in the direct vicinity of the hill and on the hill. However, the $k-\omega$ SST model manages to be closer to the experimentally obtained values. Figure 3.1.2 shows velocity profiles obtained by simulation with experimental values on different locations on the model hill for the $k-\omega$ SST turbulence model. Especially on the fine grids with 20 million and 40 million cells, the velocity profiles on the hill are very well-represented by the $k-\omega$ SST model. Further downstream of the foot of the hill, the model has some difficulties matching the experimental values.

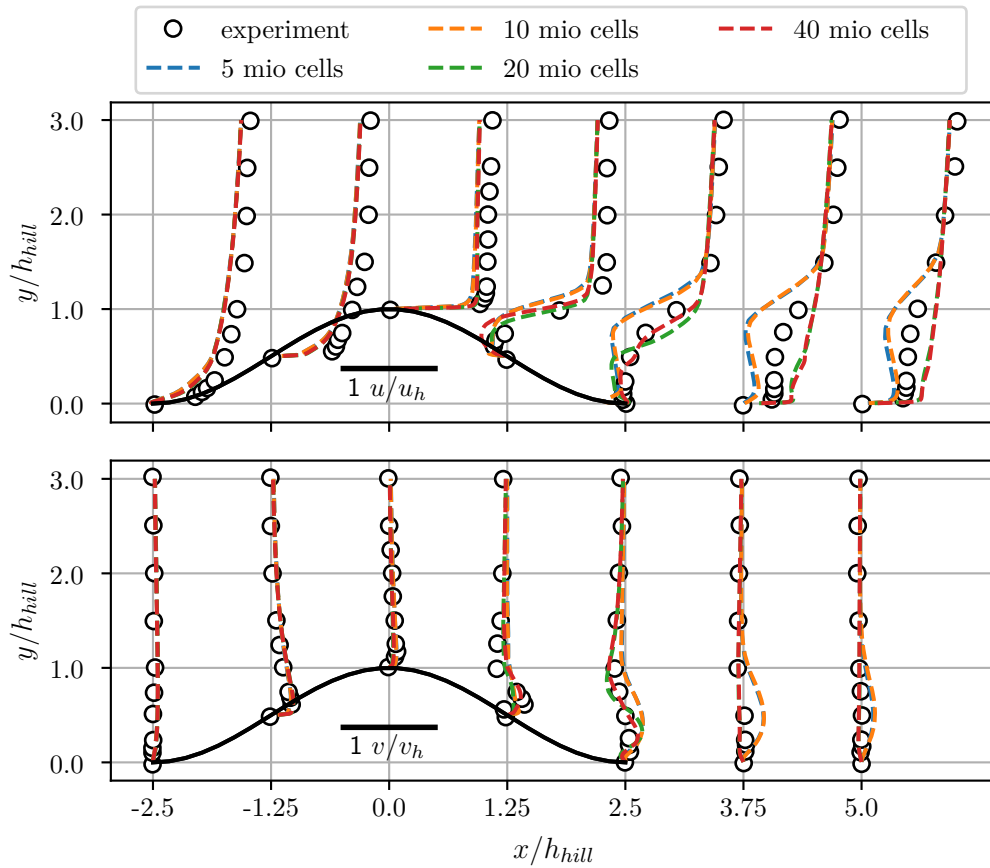


Fig. 3.1.2.: Velocity profiles at different locations in the domain. Obtained with the $k-\omega$ SST model with experimental data [58]. Horizontal velocity on the top and vertical velocity on the bottom.

Figure 3.1.3 depicts the velocity profiles obtained with the Spalart-Allmaras turbulence model. The Spalart-Allmaras turbulence model approximates the velocity profiles on the windward side and top of the hill reasonably well. On the leeward side, the general shape is captured, but it shows some lacking in the height of the wake. Especially on the foot of the hill, the Spalart-Allmaras loses accuracy in this simulation.

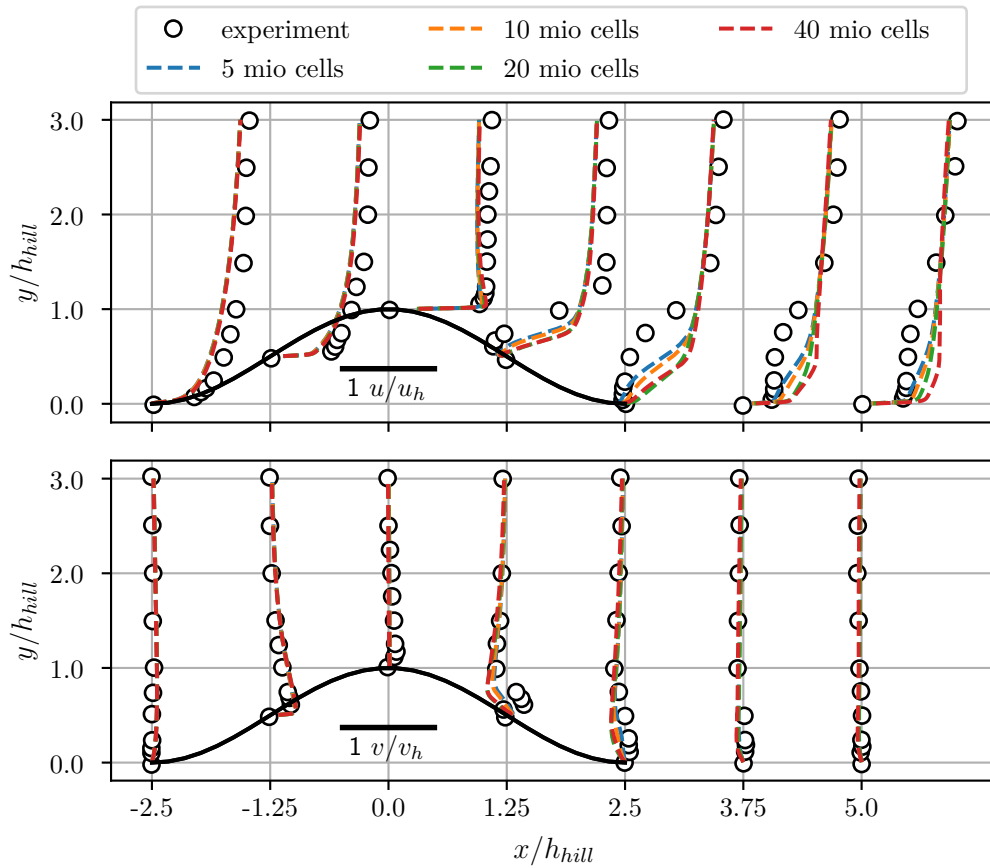


Fig. 3.1.3.: Velocity profiles at different locations in the domain. Obtained with the Spalart-Allmaras model with experimental data [58]. Horizontal velocity on the top and vertical velocity on the bottom.

3.1.2. Heat Transfer on Periodic Obstacles

The performance of ANSYS FLUENT is validated against the case described and investigated by Liu et al. [59]. In this case, periodic cubes are placed in a wind tunnel, and heated from the inside. The core of the cubes is encased by an layer of epoxy. With an infrared camera, the surface temperature was recorded. The authors also calculated the surface temperature from numerical simulations.

In accordance with the mesh by Liu et al., a structured grid is built around the cubes and in the cube's epoxy layer. However, due to its lower cell count and easier set-up, the far field is meshed with a unstructured tetrahedral mesh. The structured region around the blocks is meshed with a constant grid spacing. Using the structured mesh around the cubes as a boundary for a T-Rex mesh in POINTWISE to resolve the boundary layer on the channel wall is difficult, because the T-Rex increases the height of the cells following

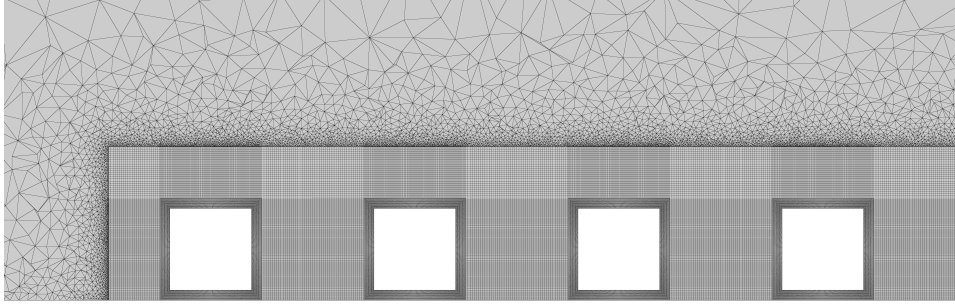


Fig. 3.1.4.: Cut through the mesh of the Liu et al. [59] validation case.

a geometric progression. Transitioning from the T-Rex to the structured mesh around the cubes usually leads to bad cell quality. Therefore, there are no prism layers in the unstructured mesh region.

The mesh resolution around the cubes is chosen to be similar to Liu et al. [59]. The cube surfaces are resolved with square cells with an edge length of 0.15 mm, the resolution perpendicular to the cube surfaces is 0.31 mm. The structured regions encasing the nine cubes consist of 22.6 million cells. The y_1^+ on the surfaces of the fifth cube does not exceed three. The combined approach to meshing with a structured mesh around the obstacles and unstructured in the far field is comparable to the hybrid mesh generated by the T-Rex algorithm.

Liu et al. calculated the case with the $k-\omega$ SST turbulence model. In this thesis, the $k-\omega$ SST and Spalart-Allmaras model are employed. The inlet boundary conditions were taken from a previous simulation. The empty wind tunnel was simulated and the velocity profile as well as the turbulent quantities at the outlet of the empty tunnel were used as the inlet boundary conditions for the validation case. The inner surface of the cubes are set at a constant temperature of $T = 243.15$ K. The heat is conducted through the epoxy layer to the outer wall of the cubes, exposed to the flow. The wall is modelled as no-slip with the heat flux as *coupled*. The heat flux through the cube surfaces is modelled via shell conduction, available in ANSYS FLUENT.

The experimental values are plotted against the simulation results in Figure 3.1.5. Although the simulation captures the general behaviour of the surface temperature, the temperature at the surface of the cube is overestimated. The discrepancies are especially high at the bottom and the back edge, as seen in the top graph. On the leading edge, the surface temperature is captured quite well. In general, the agreement between the calculation from Liu et al. [59] and the calculation done here with $k-\omega$ SST and

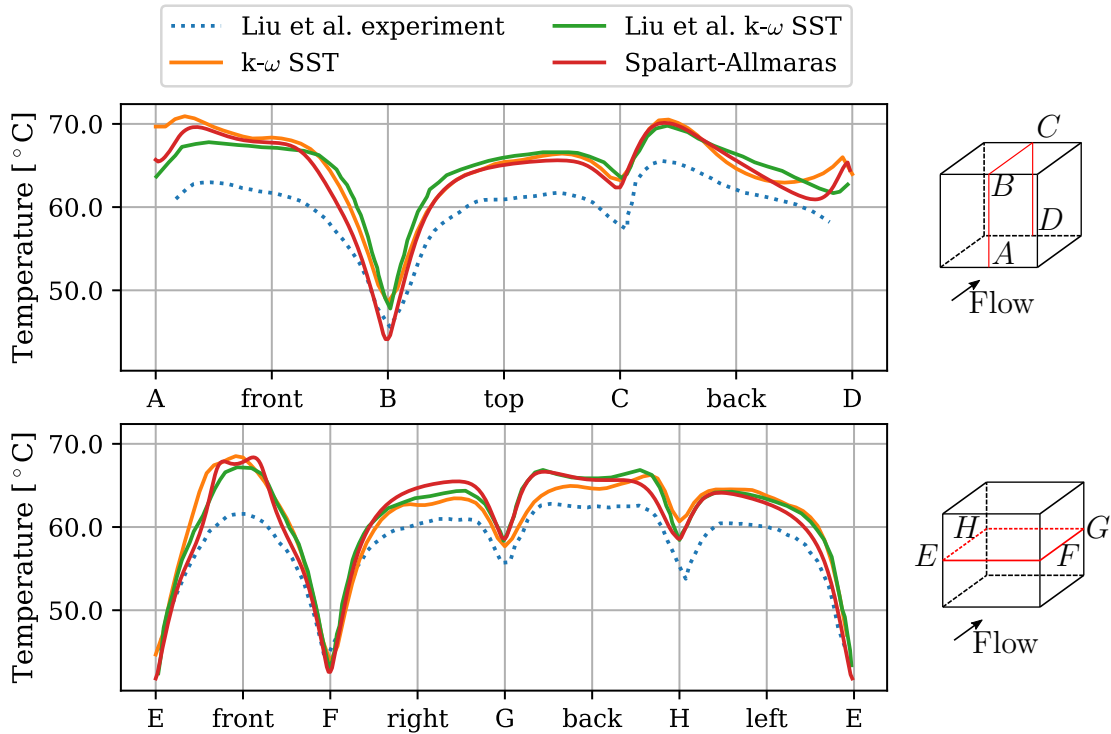


Fig. 3.1.5.: Surface temperatures on the fifth cube according to $k-\omega$ SST model and comparison with experimental and simulation data from [59].

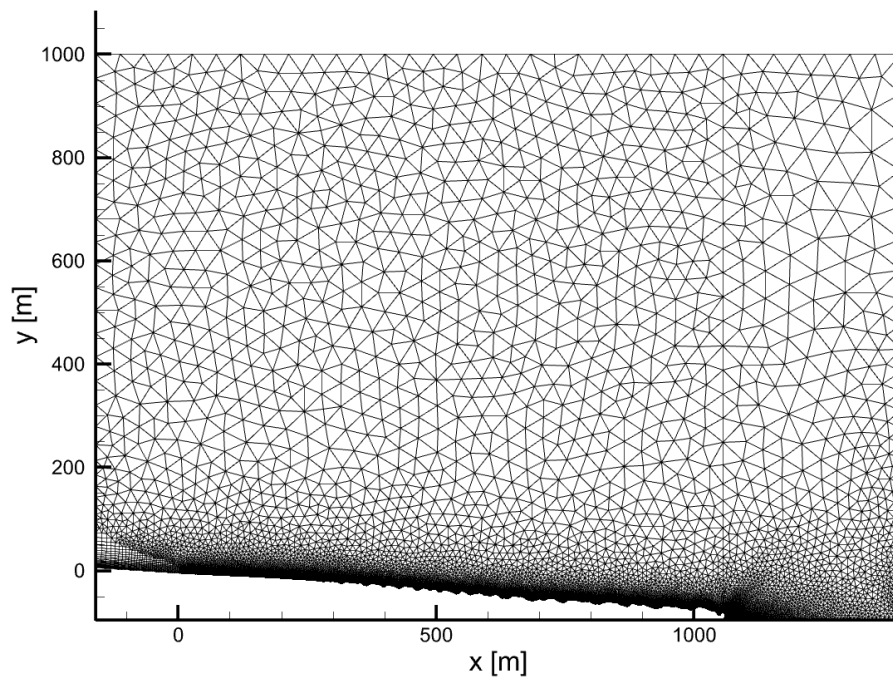
Spalart-Allmaras is quite good. Only on the bottom front and back the differences to the literature simulation are larger.

Although all simulations show quite good agreement with each other, differences in surface temperature to the experiment are apparent. As shown by Liu et al., in this case a substantially better performance for resolving surface temperature and therefore heat transfer can be achieved with LES. LES simulations usually require more computational resources and better grid resolutions and grid quality than RANS simulations. Due to computational and time restrictions as well as missing experience in LES simulations, this was unfortunately not feasible. The results given by turbulence modelling with the $k-\omega$ SST and Spalart-Allmaras models seem to be sufficient to give qualitative and reasonably accurate results to be used on the glacier geometry.

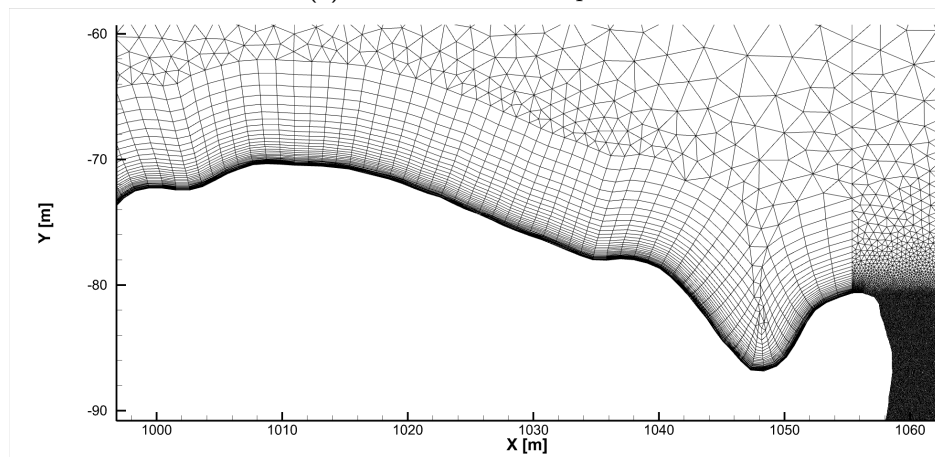
3.2. 2D Simulations

The 2D cases are meshed with the same parameters for the boundary layer resolving T-Rex mesh (see Table A.1.1). The resolution of the glacier surface between the cases is kept similar. The surface resolution is approximately 1 m.

Three different cases are investigated. For the first case, shown in Figure 3.2.1a, the wall boundary consists of the glacier surface as it is extracted from the DEM. This includes the terminus of the glacier as a near vertical drop and its downhill slope. To mitigate against the potential pressure gradient from a diffuser effect generated by the diverging top and bottom boundaries, the vertical extent is set higher than in the other two cases. This geometry is called ‘step’.

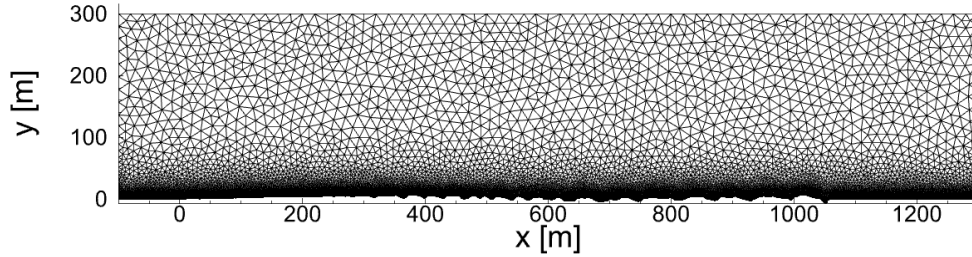


(a) Overview of the step mesh.

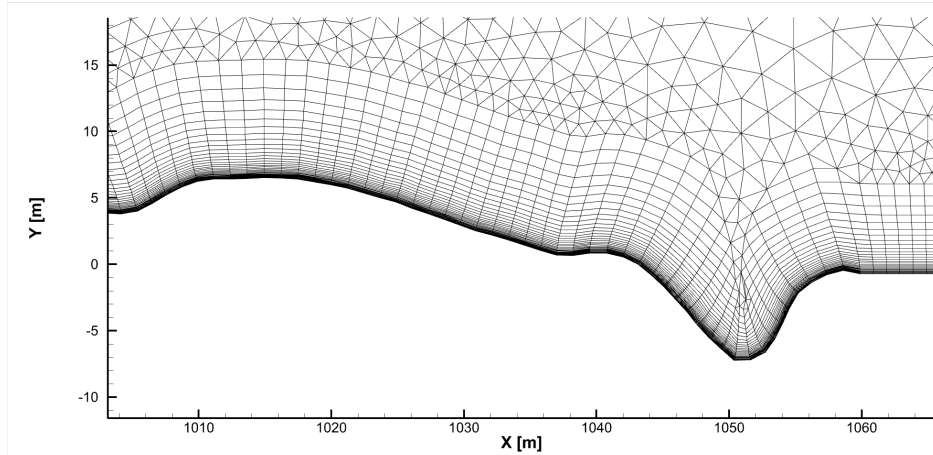


(b) Detail close with the end of the step glacier geometry.

The second case uses the same glacier surface as the step case, but omits the drop at the terminus. Furthermore, it is rotated in a way that the surface is horizontal. The mesh can be seen in Figure 3.2.2a. This geometry is called ‘flat’.



(a) Overview of the mesh.



(b) Detail of the mesh with the end of the glacier geometry at 1060 m.

Fig. 3.2.2.: Mesh of the 2D simulations for the ‘flat’ case.

Omitting the drop and turning the geometry simplifies the meshing process. It also eliminates the difficulty of increasing the resolution in the recirculation region behind the drop. It can be difficult to adequately shape the transition between cell sizes, without producing highly skewed cells. Skewed cells might inhibit numerical stability.

As a reference case, a third grid with similar extent to the flat mesh is generated. However, the bottom is purely horizontal, such that the mesh cross-section is a rectangle. This geometry is called ‘empty’.

All cases are meshed with POINTWISE using an hybrid grid. At the wall boundary the T-Rex algorithm is used to generate prism layers to resolve the boundary layer, while the far field is resolved with an unstructured mesh. For each geometry, multiple meshes are produced that mainly differ in the resolution in the wall-normal direction. While the same growth rate was used in every mesh, the initial cell height Δ_1 is varied.

For turbulence modelling, the Spalart-Allmaras model was used. It offers robust performance, while the $k-\omega$ SST model used for validation in Section 3.1 lead to numerical instability, crashing the solver.

Inlet	Velocity Inlet
Velocity Profile	$u(y) = 10 \text{ ms}^{-1} \cdot \log \frac{y}{0.1 \text{ m}} / \log \frac{10 \text{ m}}{0.1 \text{ m}}$
Temperature Profile	$T(y) = 263.15 \text{ K} - y \cdot 6.5 \text{ Kkm}^{-1}$
Turbulence Intensity	6 %
Turbulent Length Scale	5 m
Glacier Surface	no-slip Wall
Temperature (fixed)	250 K
Outlet	Pressure Outlet standard values
Top	Symmetry

Tab. 3.2.1.: Boundary conditions of the 2D cases.

The boundary conditions are set according to the methods in Section 2.5 and the same for all of the investigated cases. The chosen boundary conditions are summarized in Table 3.2.1.

3.2.1. Turbulence and Atmospheric Boundary Layer

For checking whether the chosen boundary conditions are sufficient to generate and sustain a neutrally stratified atmospheric boundary layer over a flat stretch, the case ‘empty’ is used. Consideration of the energy equation and heat transfer through the bottom wall would have influenced the boundary layer flow. Therefore the calculation is performed without taking the energy equation into account. Otherwise, the boundary conditions listed in Table 3.2.1 are employed.

The horizontal velocity profiles at the inlet and outlet of the empty domain are shown in Figure 3.2.3. Generally, the velocity profiles match reasonably well. In the lower part of the boundary layer close to the wall discrepancies are visible. Close to the surface, the velocity at the outlet is higher than at the inlet.

The profiles of the turbulent viscosity ν_t in Figure 3.2.3 do not match up well. From the inlet to the outlet, the turbulent viscosity grows. The profile of the turbulent viscosity develops a maximum around $y = 20 \text{ m}$, more closely matching expected results for flat plate boundary layers [60].

Growth of the turbulent viscosity can also be seen in the cases flat and step as is visible from Figures 3.2.4 3.2.5. Note the different scales on the color bar. The level of turbulent viscosity near the surface is generally higher in the step case, than in the flat case. It

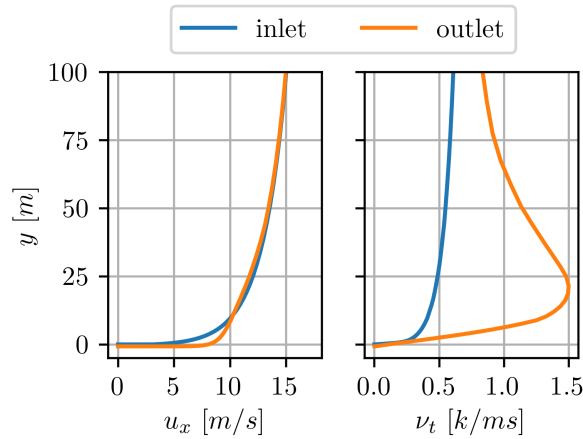


Fig. 3.2.3.: Profiles of flow quantities at the inlet and outlet of an empty 2D domain without solving the energy equation. Horizontal velocity u_x on the left, turbulent viscosity ν_t on the right. $y_1^+ \approx 4$

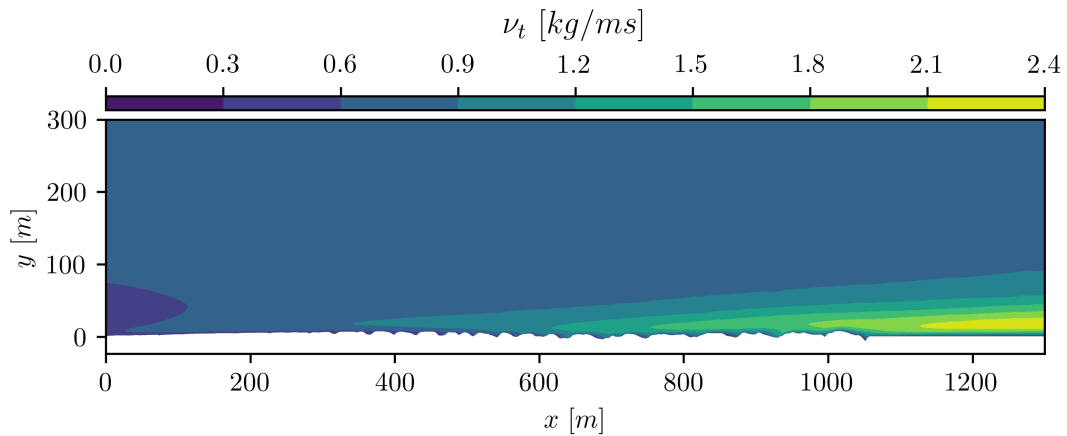


Fig. 3.2.4.: Turbulent viscosity ν_t on the flat glacier geometry with $\Delta_1 = 1$ mm.

is also notable that the terminus of the glacier geometry does not visibly impact the production of turbulence.

3.2.2. Heat Transfer

Figure 3.2.6 shows the specific heat flux on the flat glacier geometry, as well as the dimensionless height of the first cell y_1^+ and the geometry for different meshes with different initial cell heights Δ_1 at two sections of the glacier.

For both sections, the difference in heat flux on meshes with different Δ_1 and therefore y_1^+ is very small. This is the case, even though Δ_1 and y_1^+ vary by a factor of 100

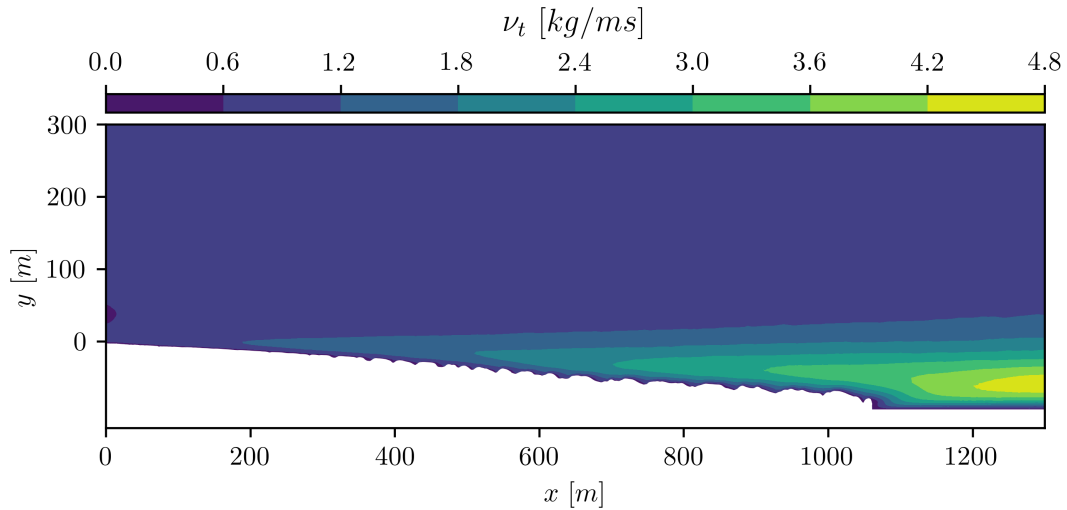


Fig. 3.2.5.: Turbulent viscosity ν_t on the step glacier geometry with $\Delta_1 = 1$ mm.

between the finest and coarsest resolution. The differences are higher on the flat section than on the more crevassed section. On both sections, the heat flux at the bottom of the crevasses and dips is substantially lower than on the surrounding geometry.

A similar behavior can be seen for the step geometry in Figure 3.2.7. The solution on the finest resolution mesh with $\Delta_1 = 0.1$ mm did not show convergence.

The specific heat flux and y_1^+ are generally roughly 40 % lower than on the flat geometry. This is probably due to a different velocity profile between these simulations.

Averages of the surface heat flux were calculated by integrating the specific heat flux along the glacier surface and dividing by the length of the interval. The results for the meshes with $\Delta_1 = 1$ mm yields the average heat fluxes shown in table 3.2.2. The table includes the averages over the sections shown in Figures 3.2.6 and 3.2.7 as well as a section closer to the terminus and the whole glacier surface from $x = 0$ m to $x = 1050$ m.

While the heat fluxes in the flat section from $x = 200$ m to 300 m between the empty and the flat geometry match closely, the step geometry is 34 % lower than on the flat geometry. Over the whole glacier surface, the step geometry shows 38 % lower heat flux than the flat geometry. Both glacier geometries show less heat flux, than the featureless empty geometry. The flat geometry shows 14 % less than the empty domain and the step geometry shows 47 % less total heat flux.

Although the differences between the two mesh geometries are apparent, both capture the same trend for the heat flux. The heat flux in the flat regions of the glacier is higher

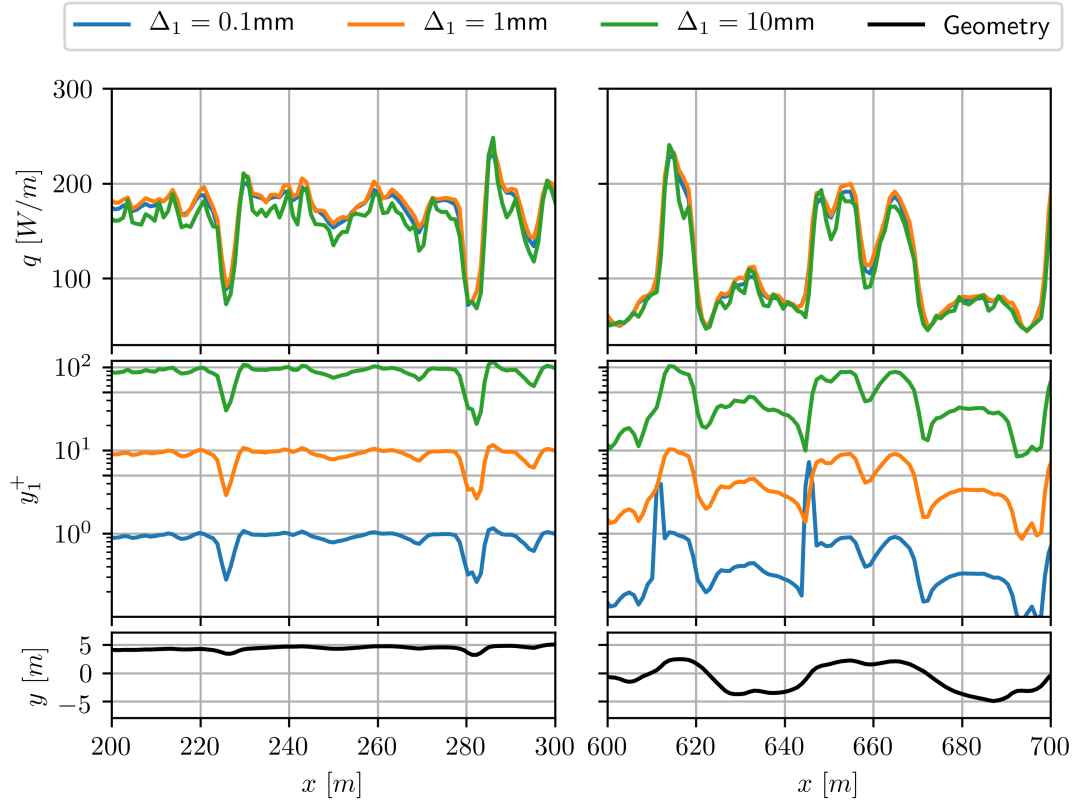


Fig. 3.2.6.: Heat flux q and y_1^+ on the flat glacier geometry. The left side shows a relatively flat part of the glacier, while the right part shows a more crevassed part. The surface contour can be seen in the bottom.

than on the crevassed regions. The highest peaks in heat flux in the crevassed regions are reached on the upstream edge of the crevasses. In the leeward sides and inside the crevasses, heat flux drops less than half in the flat case and about two thirds in the step case.

3.2.3. Velocity Profiles

Wind velocity profiles are extracted at $x = 250$ m and $x = 630$ m. Both locations are included in the sections shown in Figures 3.2.6 and 3.2.7. The position $x = 250$ m is on a relatively straight, flat section while $x = 630$ m is in the middle of a crevasse. The slope in the step case is about 5° .

The profiles shown in Figure 3.2.8 differ considerably between the cases. At the first location without a lot of crevasses, the profile for the horizontal velocity $u_{x'}$ of the step mesh differs from the velocities on the flat and empty mesh. The velocity components

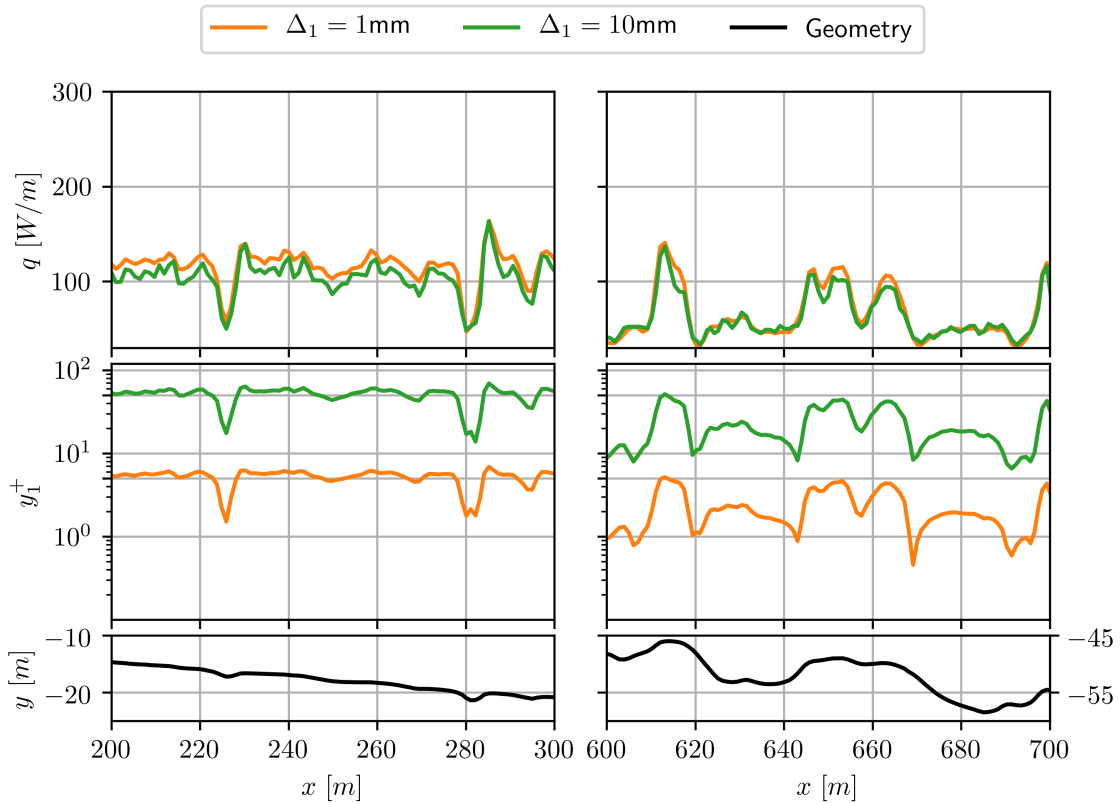


Fig. 3.2.7.: Heat flux q and y_1^+ on the step glacier geometry. The left side shows a relatively flat part of the glacier, while the right part shows a more crevassed part. The surface contour can be seen in the bottom.

of the flat and empty mesh show similar distributions. This is expected, because the surface of the glacier has no large features disturbing the flow upstream of $x = 250$ m and is therefore very similar to the empty domain.

Looking at the velocity vectors in Figure 3.2.9 shows that little flow is entering the crevasses. Most of the crevasse cross-section is covered by a recirculation zone. This leads to very low wind velocities in the crevasses as can be seen in Figure 3.2.10. Low wind velocities and recirculation inhibit the mixing with the flow above.

Fitting a logarithmic wind profile to velocity profiles obtained from the simulations gives the roughness height y_0 of the geometry. The velocities over the glacier were extracted at $x = 1060$ m on the flat geometry. This corresponds to the end of the glacier surface. The velocities of the empty case were extracted at the corresponding location. The boundary layer profiles and the fits are shown in Figure 3.2.11. Good representation of the boundary layer is achieved choosing $y_0 = 0.02$ m for the empty domain and $y_0 = 0.9$ m.

Section	Geometry		
	empty	flat	step
200 m to 300 m	172 W m^{-1}	175 W m^{-1}	115 W m^{-1}
600 m to 700 m	167 W m^{-1}	114 W m^{-1}	68 W m^{-1}
900 m to 1000 m	165 W m^{-1}	117 W m^{-1}	65 W m^{-1}
0 m to 1050 m	171 W m^{-1}	148 W m^{-1}	91 W m^{-1}

Tab. 3.2.2.: Average heat flux for the sections shown in Figures 3.2.6 and 3.2.7, an additional section close to the terminus and the whole glacier surface. Values for the investigated mesh geometries with $\Delta_1 = 1 \text{ mm}$.

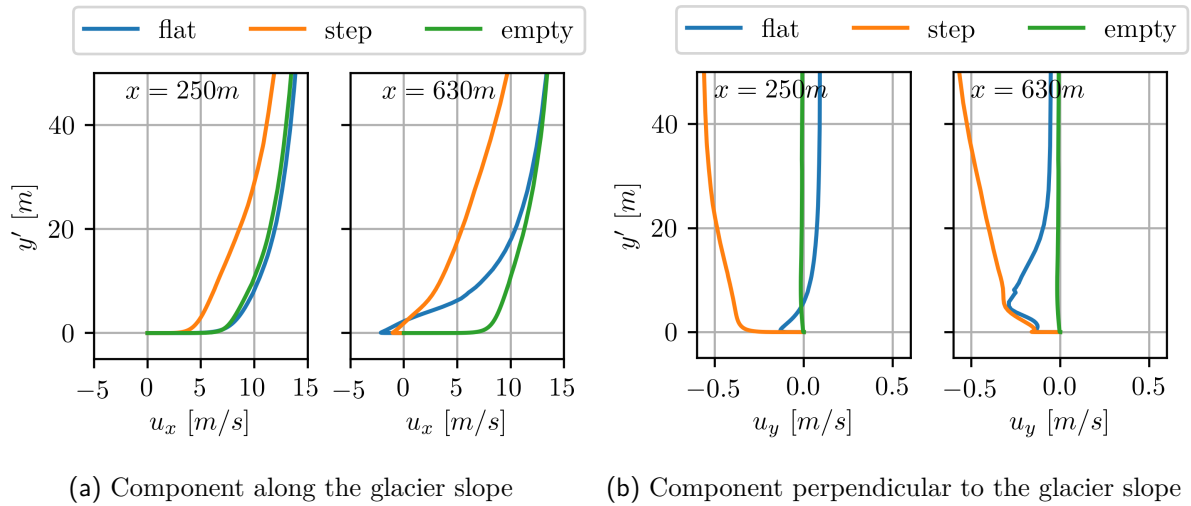


Fig. 3.2.8.: Velocity components in height y' over the glacier surface at two different locations with different cases.

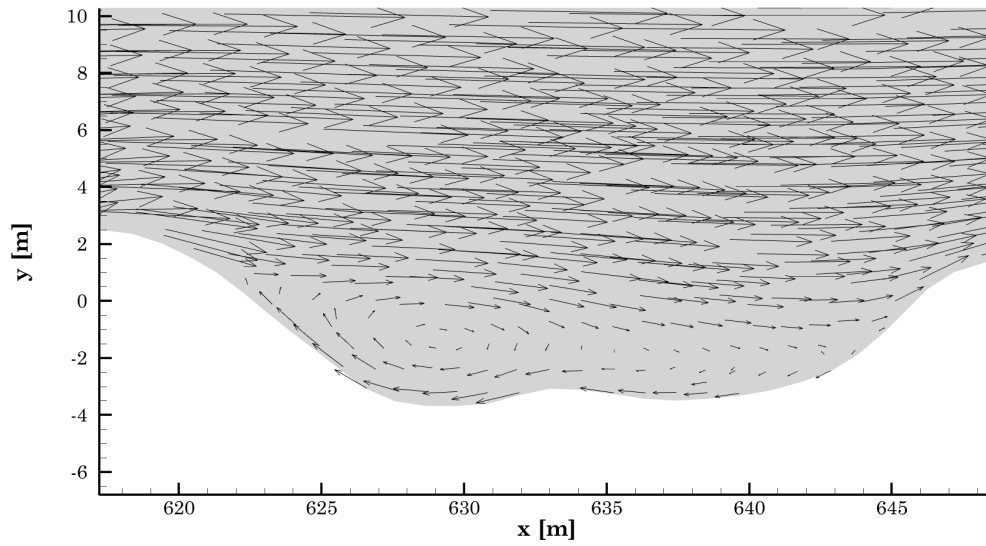


Fig. 3.2.9.: Velocity vectors in a crevasse on the flat geometry with $\Delta_1 = 1$ mm.

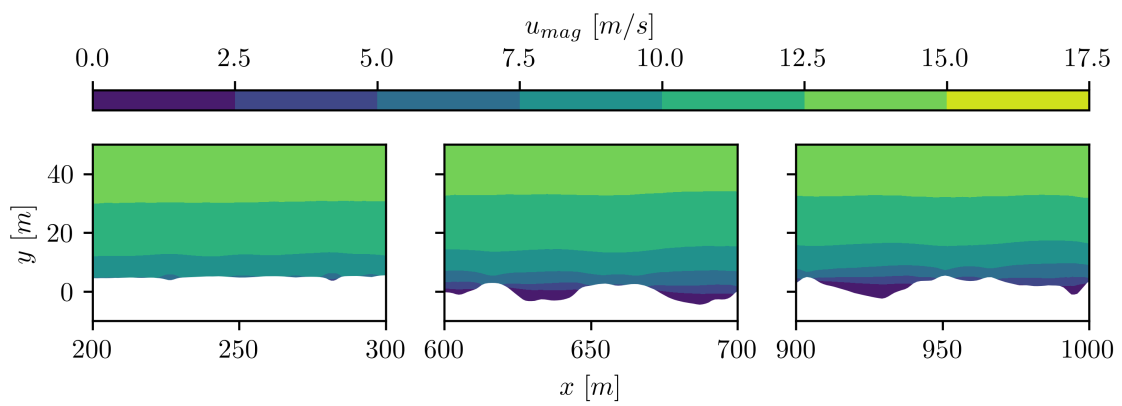


Fig. 3.2.10.: Velocity magnitude on the flat geometry in three sections.

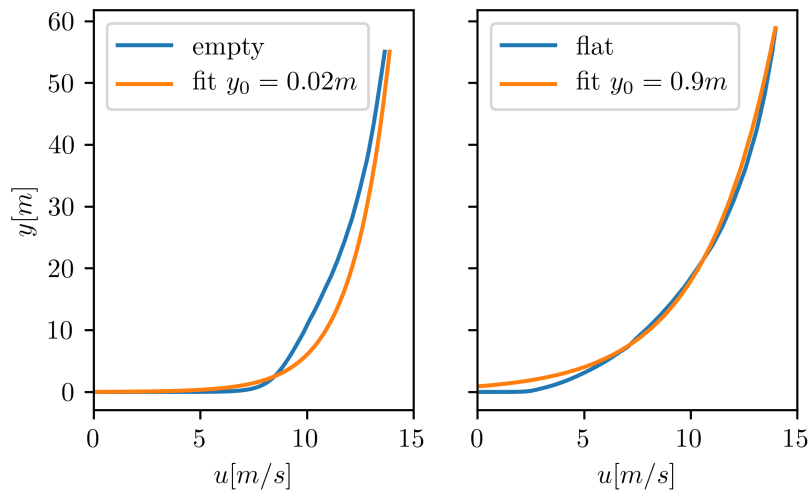


Fig. 3.2.11.: Velocity profiles and fit at $x = 1060$ m (end of the glacier).

4. Discussion

4.1. Validation

The validation cases in this thesis can only partly represent processes happening on a glacier surface. Although the case presented in Section 2.8.1 has only marginal resemblance to a glacier surface, it can be used to generally validate atmospheric boundary layer flow over an obstacles.

Especially with $k-\omega$ SST turbulence modelling, the experimental results are represented very well as seen in Figure 3.1.2. With the finer grid resolutions, the velocities on the downhill slope is captured well. The Spalart-Allmaras turbulence model still manages to capture the general structure of the flow (Figure 3.1.3), but does not match the experimental results as well as the $k-\omega$ SST model. Both models seem to be reasonably well suited for application to atmospheric boundary layer flow over obstacles. However, $k-\omega$ SST performs visibly better at detached and decelerating flows.

The case chosen for validating heat transfer (Section 3.1.2) has similarities to a glacier surface in the periodicity of the obstacles. But while on a glacier, the crevasses are reaching into the ground, the obstacles perturb into the flow in the validation case.

The Spalart-Allmaras and $k-\omega$ SST turbulence models give very similar results (Figure 3.1.5). Both overestimate the temperature on the cube surface. This is in agreement with the numerical results found by Liu et al. [59]. Liu et al. argue that $k-\omega$ SST cannot predict the flow field in the domain [59]. Judging from the very similar results between $k-\omega$ SST and Spalart-Allmaras turbulence modelling, Spalart-Allmaras seems to have similar problems. Even though both models overestimate surface temperature and therefore underestimate the heat transfer by up to 20%, they capture the trends.

Although the Spalart-Allmaras model can capture the velocity profiles in atmospheric boundary layer flow around an obstacle, it has been shown that it underestimates the turbulence intensity [61]. Using different, more complex turbulence models like $k-\omega$ SST

or the models from the $k-\varepsilon$ family could lead to more accurate flow solutions. In fact, Liu et al. found the realizable $k-\varepsilon$ to be more accurate than $k-\omega$ SST in some places. Only large eddy simulations managed to match the surface temperatures from the experiment closely [59].

Especially due to the very similar performance in the heat transfer problem, Spalart-Allmaras seems to be as well suited for the glacier problem as $k-\omega$ SST. It has to be kept in mind, that both models can capture trends, but may underestimate the heat transfer.

4.2. Glacier Simulations

The simulation carried out in this thesis were only two-dimensional. In the two-dimensional simulations, the meshing process is much easier than on the fully resolved glacier surface due to its complex with lots of convex crevasses. Although the T-Rex algorithm in POINTWISE makes it easy to generate hybrid boundary layer resolved meshes, the advancing fronts of the prism layers can lead to skewed cells. Especially in concave geometries like crevasses, the fronts can converge. POINTWISE does offer mitigations against this problem but finding the right settings proved to be challenging. When trying to mesh the three-dimensional cases with the T-Rex algorithm, no suitable mesh was achieved. Highly skewed cells were produced in the crevasses that lead to quick divergence during the calculations in ANSYS FLUENT. A more experienced user might find suitable parameters for meshing.

Although most simulations had satisfactory convergence behaviour, for the mesh with resolution $\Delta_1 = 0.1$ mm on the step geometry diverged. Most likely the reason for this was the abrupt transition from the T-Rex mesh at the end of the glacier to the unstructured mesh behind the step. This zone is also shown in Figure 3.2.1b.

The section extracted from the surface geometry follows roughly the centreline of the glacier and therefore the wind direction assumed in this thesis. As is apparent from the picture of the glacier in Figure 1.2.1, the crevasses are mostly perpendicular to the centreline and flow direction of the glacier. Therefore flow components perpendicular to the centreline should be small. In areas where the crevasses are not perpendicular to the centreline and therefore the simulation domain, a two-dimensional approach may not be sufficient for capturing the fluid flow and heat transfer correctly.

4.2.1. Atmospheric Boundary Layer

The results from the empty domain without using the glacier surface geometry in Section 3.2.1 do not show adequate representation of the atmospheric boundary layer. The velocity profile in Figure 3.2.3 shows large differences in the lower part of the boundary layer. The inlet condition described in Section 2.5.3 does not yield a distribution of turbulent viscosity that resembles a flat-plate boundary layer [60]. Along the domain, the turbulent viscosity profile develops a more typical shape.

Turbulence modelling and boundary conditions do not form a sufficient set for atmospheric boundary layer flow. Without sufficient modelling of the atmospheric boundary layer in an empty domain, changes in the velocity profile cannot be attributed only to surface roughness.

A better representation of the atmospheric boundary layer may be achieved with a different turbulence model. Richards and Norris analytically derived boundary conditions for multiple commonly turbulence models, including $k-\omega$ and $k-\varepsilon$ [23].

4.2.2. Heat Fluxes

The large differences in heat flux between the flat geometry and step geometry can be traced back to differing velocity profiles. As shown in Figure 3.2.8, the velocity close to the surface in the step case is about half the velocity close to the surface of the flat case. In the flat case, the velocity profile on the flat section of the glacier still matches the boundary layer profile of the empty case quite well. No large protrusions are upstream of the investigated point to disturb the flow. The step case does not match the boundary layer profile as closely. Furthermore, in the step case, more turbulence is produced compared to the flat case, as can be seen in Figures 3.2.4 and 3.2.5. This might be attributed to the slope of the glacier in the step case.

As seen in Figures 3.2.6 and 3.2.7 the leeward slope of the crevasses and surfaces inside the crevasse are sheltered from most of the flow on the glacier. The fluid is recirculating in the crevasse as can be seen in Figure 3.2.9. Only the downwind edge of the crevasse is impacted by the flow above, increasing heat flux locally. Down in the crevasse, the recirculation limits heat flux severely.

The low heat fluxes inside the crevasses leads to overall less heat flux in the crevassed areas. The increase in boundary layer velocity, as seen in Figure 3.2.8, and the increase

in turbulence as seen in Figures 3.2.4 and 3.2.5 cannot make up for the loss of heat transfer performance in the crevasses compared to flat sections of the glacier.

4.3. Boundary Conditions

Weather and wind conditions can change quickly and are highly dependent on the surrounding terrain. The boundary conditions in this thesis were chosen carefully but do not represent a specific weather situation. Wind profile and temperatures were chosen to be broadly representative of the arctic environment.

The atmospheric conditions above the investigated glacier are largely unknown. Extraction from model data does not provide adequately resolved data. The AROME-arctic weather model, for example, provides a spatial resolution of 2.5 km [62].

The logarithmic wind profile used as described in Section 2.5 is strictly speaking only valid on flat surfaces and driven by winds in the upper atmosphere [38]. For thermally driven winds, like the katabatic winds often found on glaciers, the wind profile is shaped differently [63].

Especially for the turbulent quantities at the inlet, little data is available. These, however, impact the performance of the simulation in recreating atmospheric boundary layers [23].

Accurate boundary conditions require on-site measurements of wind speed, temperature and, ideally, turbulence characteristics. These measurements might be relatively simple to obtain on easily accessible terrain, via remote sensing technologies like, for example, LiDAR (light detection and ranging) [64], but the usually remote glaciers and harsh environments on arctic glacier pose a big logistical problem. It could be promising to estimate the wind velocities from small, easily transportable drones like done by Garreau [13].

4.4. Geometry

Water, wind and weather constantly reshape the glacier surface on a day by day basis. Even though for a short timespan the movement of the glacier itself might be negligible, over the course of weeks or months new surface features can develop [6].

The DEM used in this thesis has a maximum resolution of 0.25 m [46]. This resolution is fine enough to capture most surface features, but limits how well crevasses can be resolved. The depth of a crevasses in the DEM can be seen as a minimum depth, because the narrow bottom might not be captured [46].

The DEM also gives no information about the material of the surface. Snow, rock and blank ice cannot be distinguished. Similarly, the surface roughness is not captured.

4.5. Modelling

The reality of heat transfer on a glacier is far more complicated than the modelling approach chosen in this thesis. The surface of glaciers is not a uniform ice sheet, but is a complex mix of snow of various textures, ice, rock, dust and in the melt season water as well. Every material and surface found on a glacier has different characteristics, for example its roughness, thermal conductivity or albedo. Especially on a local scale, these different materials are difficult to represent in a model. On land-terminating glaciers, the rocky end moraine and debris have different thermal properties than bare ice and snow further up. On sea-terminating glaciers this might be of less importance due to the missing end moraine.

Not considering phase change, like done in this thesis, cuts out all energy fluxes related to it as well as influences on the vapour content of the air. Gradients in vapour content also imply density gradients and buoyancy effects in the airflow as well as changing thermal capacity. Especially in the melt season, flowing water is common on glacier surfaces.

Heat fluxes from below the glacier and from processes in the glacier ice also influence the temperature of the ice. Temperature profiles in the ice might also depend on location in the glacier [8]. In this thesis, constant surface temperature is assumed for the glacier. Therefore, heat fluxes through the ice mass are neglected. Changing ice temperature, however, also changes thermal conductivity [6], which impacts the surface energy balance.

Although all the above mentioned effects are not accounted for in this thesis, they are still dependent on the aerodynamic flow and surface geometry. Macroscopic effects and trends in the intensity of heat transfer should still be reasonably well captured, provided that the aerodynamics is modelled accurately.



Fig. 4.5.1.: Spatial variability of surface features on a glacier. Snow, meltwater and rocks on Longyearbreen, Svalbard. Taken on 27.07.2021

4.6. Possibilities for Improvement

Both investigated cases differ in flow field as well as heat flux. Missing observations of wind and temperature profiles on glaciers make it difficult to assess the validity of the above mentioned results. Assuming the wind profile on the glacier can be represented by the logarithmic wind profile, the flat mesh manages to capture it better. The flat mesh also omits the slope of the glacier as well as the terminus. If the wind would be adequately characterized and there would not be a significant vertical gradient in air temperature and density, density currents would be included in the wind measurements. This would mean, that the slope of the glacier could be neglected and geometries similar to the flat mesh could be used.

If possible, for simulations of wind flow over terrain, the studied geometry is placed in the middle of a flat section for meshing, similar to a model in a wind tunnel (see for example [65, 66]). This way, local wind conditions do not have to be known as precisely and input from larger scale weather models can be used.

Without detailed meteorological measurements on the glacier, more of the surrounding terrain could be included in the simulation domain to get more accurate estimates for the local wind on the glacier. Model data from dominant weather situations could be used as the boundary conditions. This approach would not capture thermally driven flow which often occurs on ice sheets and glaciers [63].

Given adequate measurements, mesh geometries similar to the flat mesh should give reasonably accurate results.

4.7. Implications for Surface Energy Balance Modelling

Classical surface energy balance models use the aerodynamic roughness length to model the turbulent heat fluxes [6]. The roughness length increases in crevassed areas [46], implying more energy exchange with the atmosphere due to turbulent fluxes. The results achieved in this thesis do not support that. At least for heavily crevassed areas, recirculation zones inhibit heat transfer. Crevassed areas upwind of uncrevassed areas may increase turbulence in the flow, increasing heat transfer in downwind, uncrevassed areas.

5. Conclusion and Outlook

The CFD code ANSYS FLUENT has been validated for atmospheric boundary layer simulations using the Spalart-Allmaras and $k-\omega$ SST turbulence model. The simulation results were compared to flow around a model hill in a wind tunnel. $k-\omega$ SST performs stronger for flow around hills. Both models show deficits in predicting heat transfer on objects immersed in an atmospheric boundary layer, but do predict the trends.

For modelling heat transfer on the glacier, only turbulent fluxes were accounted for. No phase change phenomena, vapour content or liquid water was simulated.

Two different mesh geometries were investigated for heat transfer on a glacier surface. For simplicity, only two-dimensional sections were used. One mesh geometry included the terminus of the glacier as well as its slope, while in the other mesh only the surface of the glacier was rotated to be horizontal.

Comparison with an empty domain shows that the chosen boundary conditions for the Spalart-Allmaras turbulence model were not sufficient to sustain a neutral atmospheric boundary layer throughout the domain. For the heat flux large differences between the investigated geometries were found. With different vertical resolutions for the same mesh geometry, the heat fluxes were not differing substantially.

Differences in heat flux between the mesh geometries can be attributed to differing fluid flow. It seems likely that the flat mesh geometry is the more accurate solution. However, for accurate results the wind conditions on the glacier should be better characterized to achieve better inflow conditions. Furthermore, the use of a different turbulence model, like for example $k-\omega$ SST could improve the accuracy of the aerodynamic modelling.

Even though Spalart-Allmaras and $k-\omega$ SST underestimate the heat transfer and results between mesh geometries differ, the simulations show clearly a reduction in aerodynamic heat flux in the crevassed region compared to flat regions on the glacier. The air inside the crevasse recirculates such that no efficient heat transfer is possible. This raises

questions regarding the traditional approach to surface energy balance modelling, where higher roughness is equated to higher heat fluxes due to turbulent mixing.

For further investigations into surface energy balance with CFD it would be advantageous to characterize the common wind patterns and temperatures on the glacier of interest to have better estimates for boundary conditions. Although 2D simulations are already giving insights into the trends of surface heat flux, 3D simulations can give spatially resolved results. These results could be used to improve existing surface energy balance models.

Bibliography

- [1] R.K. Pachauri, L. M., ed. *Climate Change 2014: Synthesis Report. Contribution of Working Groups I, II and III to the Fifth Assessment Report of the Intergovernmental Panel on Climate Change*. Geneva, 2014 (cit. on p. 1).
- [2] Doran, P. T. and Zimmerman, M. K. ‘Examining the Scientific Consensus on Climate Change’. In: 90 (2009), p. 22 (cit. on p. 1).
- [3] Adakudlu, M., Andresen, J., Bakke, J., Beldring, S., Benestad, R., Bilt, W. v. d., Bogen, J., Borstad, C. P., Breili, K., Breivik, Ø. et al. *Climate in Svalbard 2100*. 2019 (cit. on p. 1).
- [4] Dutton, A., Carlson, A. E., Long, A. J., Milne, G. A., Clark, P. U., DeConto, R., Horton, B. P., Rahmstorf, S. and Raymo, M. E. ‘Sea-level rise due to polar ice-sheet mass loss during past warm periods’. In: *Science* 349.6244 (July 2015), aaa4019–aaa4019 (cit. on p. 1).
- [5] Lenaerts, J. T. M., Bars, D. L., Kampenhout, L. van, Vizcaino, M., Enderlin, E. M. and Broeke, M. R. van den. ‘Representing Greenland ice sheet freshwater fluxes in climate models’. In: *Geophysical Research Letters* 42.15 (Aug. 2015), pp. 6373–6381 (cit. on p. 1).
- [6] Benn, D. and Evans, D. J. *Glaciers and glaciation*. Routledge, 2014 (cit. on pp. 1–3, 39, 40, 42).
- [7] Veen, C. J. van der. ‘Crevasses on Glaciers’. In: *Polar Geography* 23.3 (July 1999), pp. 213–245 (cit. on p. 2).
- [8] Cuffey, K. M. and Paterson, W. S. B. *The physics of glaciers*. Academic Press, 2010 (cit. on pp. 2, 3, 40).
- [9] Munro, D. S. ‘Surface roughness and bulk heat transfer on a glacier: comparison with eddy correlation’. In: *Journal of Glaciology* 35.121 (1989), pp. 343–348 (cit. on p. 2).

- [10] Arnold, N. ‘Investigating the Sensitivity of Glacier Mass-Balance/Elevation Profiles to Changing Meteorological Conditions: Model Experiments for Haut Glacier D’Arolla, Valais, Switzerland’. In: *Arctic, Antarctic, and Alpine Research* 37.2 (May 2005), pp. 139–145 (cit. on p. 2).
- [11] Fausto, R. S., As, D., Box, J. E., Colgan, W., Langen, P. L. and Mottram, R. H. ‘The implication of nonradiative energy fluxes dominating Greenland ice sheet exceptional ablation area surface melt in 2012’. In: *Geophysical Research Letters* 43.6 (Mar. 2016), pp. 2649–2658 (cit. on p. 3).
- [12] Dachauer, A., Hann, R. and Hodson, A. J. ‘Aerodynamic roughness length of crevassed tidewater glaciers from UAV mapping’. In: *The Cryosphere Discussions* (May 2021) (cit. on pp. 3, 13, 15).
- [13] Garreau, A. ‘Validation and Application of Novel Wind Estimation Methods with Quadcopter UAVs in the Arctic’. MA thesis. The University Center in Svalbard and École Nationale de la Météorologie, 2020 (cit. on pp. 3, 39).
- [14] Blazek, J. *Computational fluid dynamics: principles and applications*. 3rd ed. Amsterdam San Diego: Butterworth Heinemann, 2015 (cit. on pp. 6, 8, 9).
- [15] *Pointwise Inc. Website*. URL: <https://www.pointwise.com/> (visited on 14/06/2021) (cit. on p. 6).
- [16] Steinbrenner, J. P. ‘Construction of Prism and Hex Layers from Anisotropic Tetrahedra’. In: *22nd AIAA Computational Fluid Dynamics Conference*. American Institute of Aeronautics and Astronautics, June 2015 (cit. on p. 7).
- [17] Anderson Jr, J. D. *Fundamentals of aerodynamics*. 1st ed. Tata McGraw-Hill Education, 2010 (cit. on p. 7).
- [18] Oertel jr., H., ed. *Prandtl – Führer durch die Strömungslehre: Grundlagen und Phänomene*. Deutsch. 14. Aufl. 2017. Springer Reference Technik. Wiesbaden: Springer Vieweg, 2017 (cit. on pp. 8, 13).
- [19] Leschziner, M. and Drikakis, D. ‘Turbulence modelling and turbulent-flow computation in aeronautics’. In: *Aeronautical Journal* 106.1061 (2002), pp. 349–384 (cit. on pp. 8, 9).
- [20] Wilcox, D. C. ‘Formulation of the $k-\omega$ Turbulence Model Revisited’. In: *AIAA Journal* 46.11 (Nov. 2008), pp. 2823–2838 (cit. on pp. 8–12).
- [21] Lamanna, G. and Spring, S. *Applied Turbulence Modelling. Lecture Notes*. 2019 (cit. on pp. 8, 10).

- [22] Younis, B. *Applied Turbulence Modelling. Lecture Notes*. 1st Sept. 2002 (cit. on p. 9).
- [23] Richards, P. and Norris, S. ‘Appropriate boundary conditions for computational wind engineering models revisited’. In: *Journal of Wind Engineering and Industrial Aerodynamics* 99.4 (Apr. 2011), pp. 257–266 (cit. on pp. 9, 13, 14, 17, 38, 39).
- [24] Pope, S. B. *Turbulent flows*. Englisch. Ed. by Pope, S. B. [Cambridge Univ. Pr., 2009, XXXIV, 771 Seiten (cit. on p. 9).
- [25] Ansys Inc. *Ansys Fluent 2020R1 Theory Guide* (cit. on pp. 9–12).
- [26] Launder, B. E. and Spalding, D. B. ‘The numerical computation of turbulent flows’. In: *Numerical prediction of flow, heat transfer, turbulence and combustion*. Elsevier, 1983, pp. 96–116 (cit. on p. 10).
- [27] Franke, J., Hirsch, C., Jensen, A., Krüs, H., Schatzmann, M., Westbury, P., Miles, S., Wisse, J. and Wright, N. ‘Recommendations on the use of CFD in predicting pedestrian wind environment’. In: *Cost action C*. Vol. 14. 2004 (cit. on p. 10).
- [28] Yakhot, V., Orszag, S., Thangam, S., Gatski, T. and Speziale, C. ‘Development of turbulence models for shear flows by a double expansion technique’. In: *Physics of Fluids A: Fluid Dynamics* 4.7 (1992), pp. 1510–1520 (cit. on p. 10).
- [29] Shih, T., Liou, W., Shabbir, A., Yang, Z. and Zhu, J. ‘A new k- ϵ eddy viscosity model for high Reynolds number turbulent flows-Model development and validation’. In: *NASA TM* 106721 (1994) (cit. on p. 10).
- [30] Kolmogorov, A. N. ‘Equations of turbulent motion in an incompressible fluid’. In: *Dok. Akad. Nauk SSSR*. Vol. 30. 1941, pp. 299–303 (cit. on p. 11).
- [31] Wilcox, D. C. *Turbulence Modeling for CFD (Third Edition)*. 3rd ed. Dcw Industries, Incorporated, 2006 (cit. on p. 11).
- [32] Wilcox, D. C. ‘Reassessment of the scale-determining equation for advanced turbulence models’. In: *AIAA journal* 26.11 (1988), pp. 1299–1310 (cit. on p. 11).
- [33] Menter, F. R., Kuntz, M. and Langtry, R. ‘Ten years of industrial experience with the SST turbulence model’. In: *Turbulence, heat and mass transfer* 4.1 (2003), pp. 625–632 (cit. on pp. 11, 12).
- [34] Menter, F. R. ‘Two-equation eddy-viscosity turbulence models for engineering applications’. In: *AIAA journal* 32.8 (1994), pp. 1598–1605 (cit. on p. 11).
- [35] Menter, F. R. ‘Influence of freestream values on k- ω turbulence model predictions’. In: *AIAA journal* 30.6 (1992), pp. 1657–1659 (cit. on p. 11).

- [36] Spalart, P. and Allmaras, S. ‘A one-equation turbulence model for aerodynamic flows’. In: *30th Aerospace Sciences Meeting and Exhibit*. American Institute of Aeronautics and Astronautics, Jan. 1992 (cit. on p. 12).
- [37] Hargreaves, D. and Wright, N. ‘On the use of the $k-\varepsilon$ model in commercial CFD software to model the neutral atmospheric boundary layer’. In: *Journal of Wind Engineering and Industrial Aerodynamics* 95.5 (May 2007), pp. 355–369 (cit. on pp. 13, 14).
- [38] Kraus, H. *Grundlagen der Grenzschicht-Meteorologie*. Springer Berlin Heidelberg, 2008 (cit. on pp. 13, 14, 39).
- [39] Walshe, J. ‘CFD modelling of wind flow over complex and rough terrain’. PhD thesis. Loughborough University, 2003 (cit. on p. 13).
- [40] International Organization for Standardization. *ISO 2533: Standard Atmosphere*. 1975 (cit. on p. 14).
- [41] Gardner, A. S., Sharp, M. J., Koerner, R. M., Labine, C., Boon, S., Marshall, S. J., Burgess, D. O. and Lewis, D. ‘Near-Surface Temperature Lapse Rates over Arctic Glaciers and Their Implications for Temperature Downscaling’. In: *Journal of Climate* 22.16 (Aug. 2009), pp. 4281–4298 (cit. on p. 14).
- [42] Aas, K. S., Berntsen, T. K., Boike, J., Eitzelmüller, B., Kristjánsson, J. E., Maturilli, M., Schuler, T. V., Stordal, F. and Westermann, S. ‘A Comparison between Simulated and Observed Surface Energy Balance at the Svalbard Archipelago’. In: *Journal of Applied Meteorology and Climatology* 54.5 (May 2015), pp. 1102–1119 (cit. on p. 14).
- [43] Ansys Inc. *Ansys Fluent 2020R1 User’s Guide* (cit. on pp. 14, 15).
- [44] Türk, M. and Emeis, S. ‘The dependence of offshore turbulence intensity on wind speed’. In: *Journal of Wind Engineering and Industrial Aerodynamics* 98.8-9 (Aug. 2010), pp. 466–471 (cit. on p. 15).
- [45] Baehr, H. D. and Stephan, K. *Wärme- und Stoffübertragung*. Springer Berlin Heidelberg, 2019 (cit. on p. 15).
- [46] Dachauer, A. ‘Aerodynamic Roughness Length of Crevassed Tideater Glaciers from UAV Mapping’. MA thesis. Institute for Atmospheric and Climate Science, Department of Earth Sciences, ETH Zürich, 19th Oct. 2020 (cit. on pp. 16, 40, 42).
- [47] Norwegian Polar Institute. *Toposvalbard*. URL: <http://www.toposvalbard.npolar.no> (visited on 30/06/2021) (cit. on p. 16).

- [48] Hirt, C. ‘Digital Terrain Models’. In: *Encyclopedia of Geodesy*. Ed. by Grafarend, E. Cham: Springer International Publishing, 2014, pp. 1–6 (cit. on p. 15).
- [49] Roache, P. J. ‘Quantification of Uncertainty in Computational Fluid Dynamics’. In: *Annual Review of Fluid Mechanics* 29.1 (Jan. 1997), pp. 123–160 (cit. on p. 16).
- [50] Politis, E. S., Prospathopoulos, J., Cabezón, D., Hansen, K. S., Chaviaropoulos, P. K. and Barthelmie, R. J. ‘Modeling wake effects in large wind farms in complex terrain: the problem, the methods and the issues’. In: *Wind Energy* 15.1 (Aug. 2011), pp. 161–182 (cit. on p. 16).
- [51] Peralta, C., Nugusse, H., Kokilavani, S., Schmidt, J. and Stoevesandt, B. ‘Validation of the simplefoam (rans) solver for the atmospheric boundary layer in complex terrain’. In: *ITM Web of Conferences*. Vol. 2. EDP Sciences. 2014, p. 01002 (cit. on p. 16).
- [52] Rodrigo, J. S., Gancarski, P., Arroyo, R. C., Moriarty, P., Chuchfield, M., Naughton, J. W., Hansen, K. S., Machefaux, E., Koblitiz, T., Maguire, E. et al. ‘Iea-task 31 wakebench: Towards a protocol for wind farm flow model evaluation. part 1: Flow-over-terrain models’. In: *Journal of Physics: Conference Series*. Vol. 524. 1. IOP Publishing. 2014, p. 012105 (cit. on p. 16).
- [53] Dhunny, A., Lollchund, M. and Rughooputh, S. ‘Wind energy evaluation for a highly complex terrain using Computational Fluid Dynamics (CFD)’. In: *Renewable Energy* 101 (Feb. 2017), pp. 1–9 (cit. on p. 16).
- [54] Plate, E. J. ‘Methods of investigating urban wind fields—physical models’. In: *Atmospheric Environment* 33.24-25 (Oct. 1999), pp. 3981–3989 (cit. on p. 16).
- [55] Taylor, P. and Teunissen, H. ‘The Askervein Hill project: overview and background data’. In: *Boundary-layer meteorology* 39.1-2 (1987), pp. 15–39 (cit. on p. 17).
- [56] Berg, J., Mann, J., Bechmann, A., Courtney, M. and Jørgensen, H. E. ‘The Bolund experiment, part I: flow over a steep, three-dimensional hill’. In: *Boundary-layer meteorology* 141.2 (2011), p. 219 (cit. on p. 17).
- [57] DTU Wind Energy. *Bolund Hill Data*. URL: <https://www.bolund.vindenergi.dtu.dk/> (visited on 23/11/2020) (cit. on p. 17).
- [58] Ishihara, T., Hibi, K. and Oikawa, S. ‘A wind tunnel study of turbulent flow over a three-dimensional steep hill’. In: *Journal of Wind Engineering and Industrial Aerodynamics* 83.1-3 (Nov. 1999), pp. 95–107 (cit. on pp. 17–22).

- [59] Liu, J., Srebric, J. and Yu, N. ‘Numerical simulation of convective heat transfer coefficients at the external surfaces of building arrays immersed in a turbulent boundary layer’. In: *International Journal of Heat and Mass Transfer* 61 (June 2013), pp. 209–225 (cit. on pp. 17–19, 22–24, 36, 37).
- [60] Schlichting, H. and Gersten, K., eds. *Grenzschicht-Theorie*. Deutsch. Berlin, Heidelberg, 2006 (cit. on pp. 28, 38).
- [61] Chwalowski, P. and Ivanco, T. G. ‘Modeling of an Atmospheric-Boundary-Layer Profile in Support of Experiments in the NASA Langley Transonic Dynamics Tunnel’. In: *International Forum on Aeroelasticity and Structural Dynamics*. 2019-027. 2019 (cit. on p. 36).
- [62] Norwegian Meteorological Institute. *The AROME-Arctic weather model*. URL: <https://www.met.no/en/projects/The-weather-model-AROME-Arctic> (visited on 28/06/2021) (cit. on p. 39).
- [63] Manins, P. C. and Sawford, B. L. ‘A Model of Katabatic Winds’. In: *Journal of the Atmospheric Sciences* 36.4 (Apr. 1979), pp. 619–630 (cit. on pp. 39, 41).
- [64] Krishnamurthy, R., Calhoun, R., Billings, B. and Doyle, J. ‘Wind turbulence estimates in a valley by coherent Doppler lidar’. In: *Meteorological Applications* 18.3 (Aug. 2011), pp. 361–371 (cit. on p. 39).
- [65] Blocken, B., Hout, A. van der, Dekker, J. and Weiler, O. ‘CFD simulation of wind flow over natural complex terrain: Case study with validation by field measurements for Ria de Ferrol, Galicia, Spain’. In: *Journal of Wind Engineering and Industrial Aerodynamics* 147 (Dec. 2015), pp. 43–57 (cit. on p. 41).
- [66] Conan, B., Chaudhari, A., Aubrun, S., Beeck, J. van, Hämäläinen, J. and Hellsten, A. ‘Experimental and Numerical Modelling of Flow over Complex Terrain: The Bolund Hill’. In: *Boundary-Layer Meteorology* 158.2 (Sept. 2015), pp. 183–208 (cit. on p. 41).

A. Appendix: Set-up and Grids

A.1. 2D Glacier

A.1.1. Meshes

The meshes for the flat and step case as described in [3.2.2](#) have been set up to closely resemble each other. The T-Rex parameters for both cases are shown in table [A.1.1](#).

A.1.2. Solver Set-Up and Boundary Conditions

Especially with the step cases, the turbulent viscosity gets bigger than the standard limits in the code. These limits can be set in the *Controls* panel under *Limits* in ANSYS FLUENT. If convergence problems arise, setting the under-relaxation of the turbulent viscosity ratio to values less than 1, e.g. 0.8 may lead to convergence.

Max Layers	80
Full Layers	12
Growth Rate	1.15

Tab. A.1.1.: T-Rex set-up for flat and step case

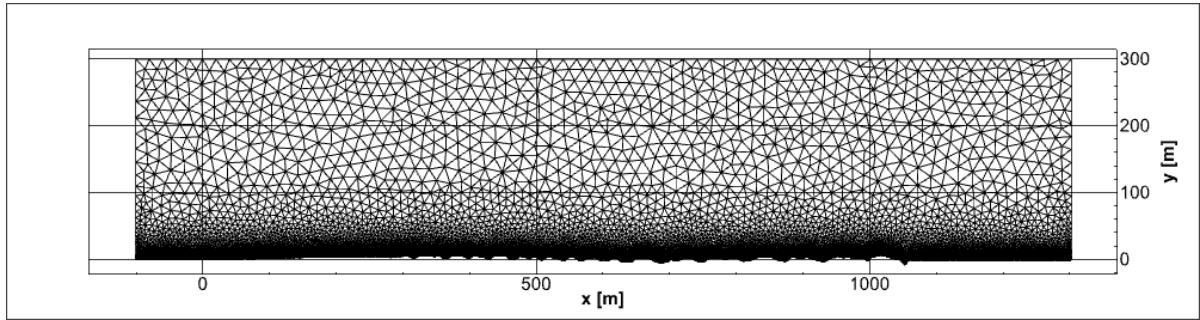


Fig. A.1.1.: Overview of the flat mesh.

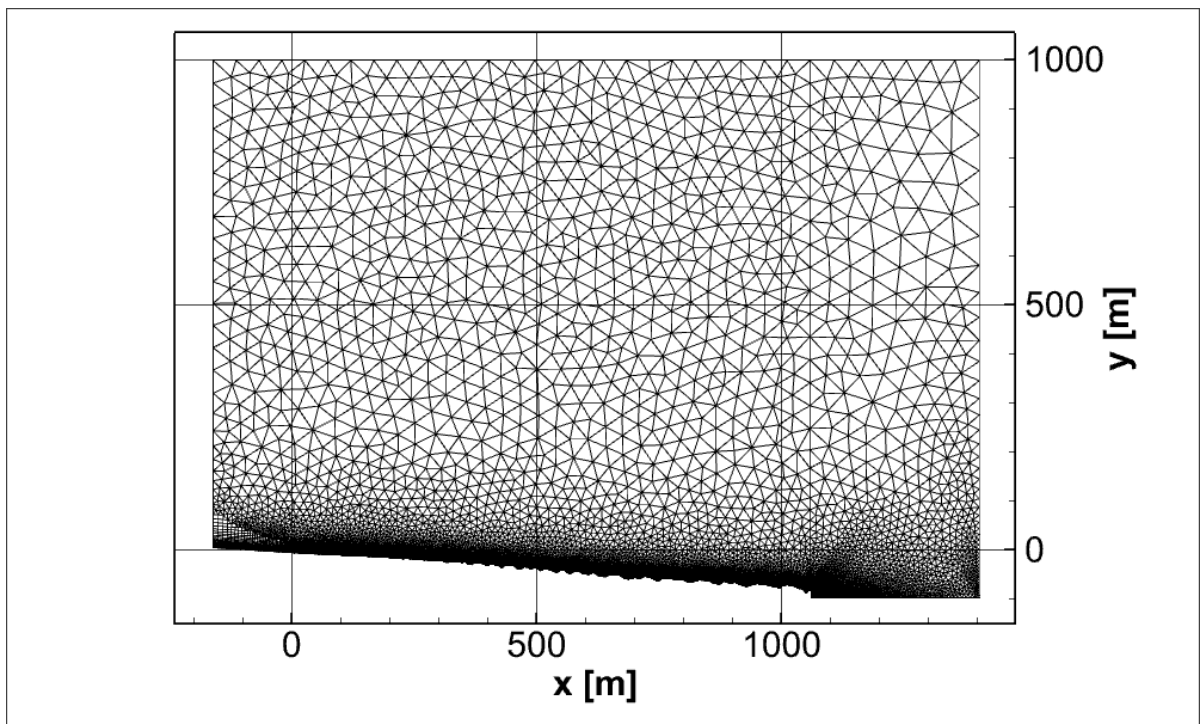


Fig. A.1.2.: Overview of the step mesh.

Inlet	Velocity Inlet
Outlet	Pressure Outlet
Sides	Symmetry
Glacier Surface	Wall

Tab. A.1.2.: Boundary conditions for flat and step case

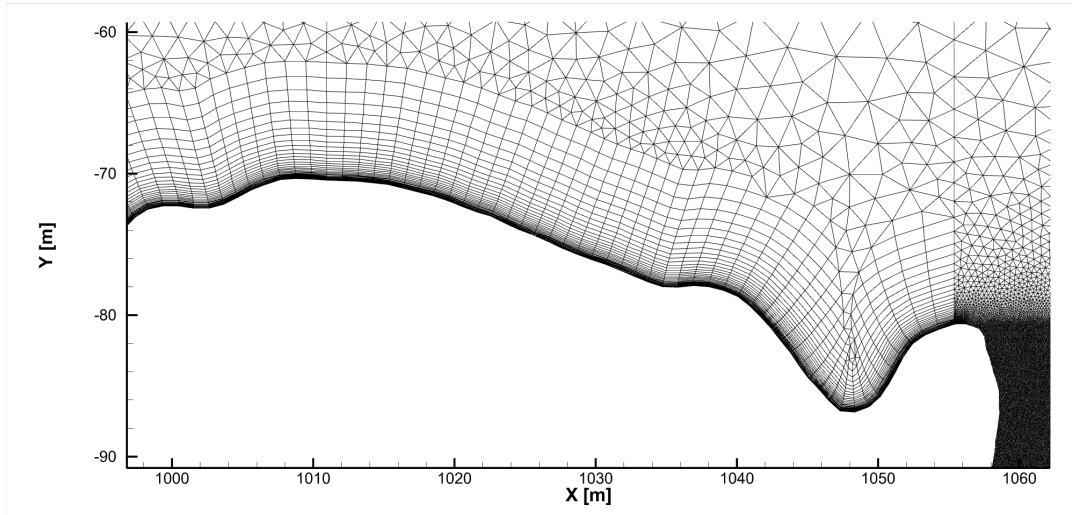


Fig. A.1.3.: Detail close with the end of the step glacier geometry.

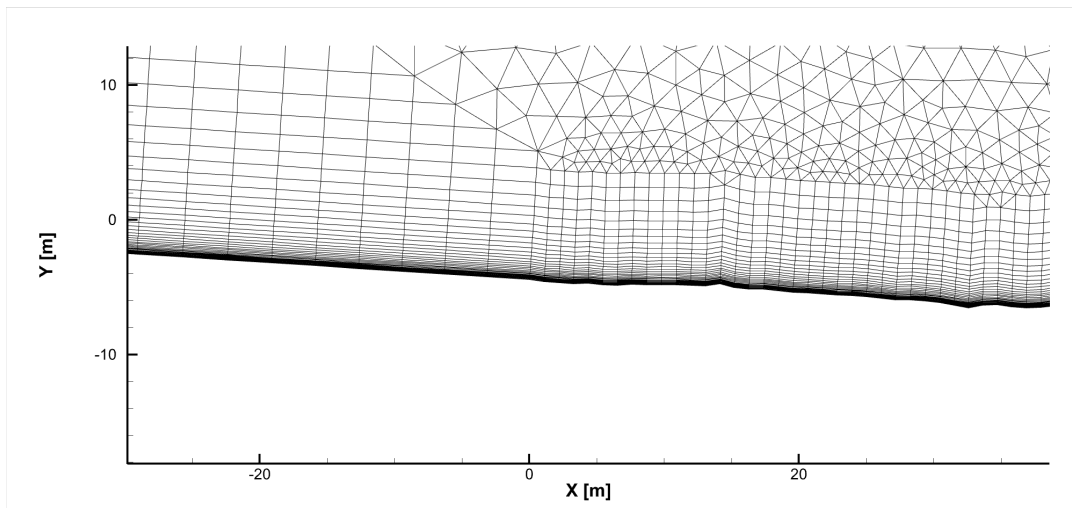


Fig. A.1.4.: Detail at the beginning of the step glacier geometry at 0 m.

Spatial Discretization	
Pressure	Second Order
Momentum	Second Order Upwind
Modified Turbulent Viscosity	Second Order Upwind
Pressure-Velocity Coupling	SIMPLE

Tab. A.1.3.: Solver set-up for 2D glacier cases.